

Upstream Orographic Enhancement of a Narrow Cold-Frontal Rainband Approaching the Andes

MAXIMILIANO VIALE*

Instituto Argentino de Nivología, Glaciología y Ciencias Ambientales (IANIGLA), CCT-CONICET, Mendoza, Argentina

ROBERT A. HOuze JR. AND KRISTEN L. RASMUSSEN

Department of Atmospheric Sciences, University of Washington, Seattle, Washington

(Manuscript received 10 May 2012, in final form 7 September 2012)

ABSTRACT

Upstream orographic enhancement of the rainfall from an extratropical cyclone approaching the Andes from the Pacific is investigated using the Weather Research and Forecasting (WRF) Model and the Tropical Rainfall Measuring Mission (TRMM) Precipitation Radar. The main precipitation from the cyclone over central and coastal Chile fell when a narrow cold-frontal rainband (NCFR) interacted with a midlevel layer cloud deck formed from the orographically induced ascent of the prefrontal “atmospheric river” upstream of the Andes. Model output indicates that low-level convergence enhanced the NCFR where it met low-level blocked flow near the mountains. The NCFR had stronger updrafts with decreasing distance from the mountains, and the NCFR produced larger rain accumulations over the land region upstream of the Andes than over the open ocean. A sensitivity simulation with a 50% reduction in the Andes topography, for comparison to various west coast mountain ranges of North America, demonstrates that the extreme height of the real mountain barrier strengthens frontogenesis and upstream blocking, which produces stronger frontal lifting and a slower progression of the frontal system. The model and the satellite data suggest that the larger precipitation rates upstream of the Andes resulted from a seeder–feeder effect connected with the orographically invigorated NCFR updrafts, when they penetrated the orographically enhanced midlevel stratiform clouds forming as a result of the upstream orographic ascent of the atmospheric river. The supercooled water of the NCFR updrafts formed a feeder zone for the snow particles in the midlevel stratiform cloud just upstream of the Andes.

1. Introduction

The great height and steepness of the Andes and their extremely long meridional extent profoundly alter the precipitation systems from midlatitude cyclones approaching South America. Mean wintertime observations show a marked cross-barrier gradient of precipitation in the region of the central Andes [$\sim(30^{\circ}\text{--}37^{\circ}\text{S})$], with orographic precipitation enhancement on the windward slopes of the Chilean side and a prominent rain-shadow

effect on the leeward slopes of the Argentinean side (Viale and Nuñez 2011; Falvey and Garreaud 2007). Over the lowlands of central Chile and the adjacent Pacific coast, blocking by the Andes leads to stronger convergence of passing surface fronts and enhanced upstream precipitation (Barrett et al. 2009). The physical mechanism of the precipitation enhancement has, however, not been explored. The main purpose of this paper is to explore this process.

Field experiments have investigated upstream blocking effects on frontal precipitation along the mountainous coasts of Oregon and California. The California Land-falling Jets Experiment (CALJET; Ralph et al. 1999; Neiman et al. 2004) showed that low-level blocking has a strong impact on rainfall distributions, often leading to orographically enhanced flooding in the region. In field experiments over the mountainous coasts of Washington, Oregon, and northern California, airborne

* Current affiliation: Departamento de Geofísica, Universidad de Chile, Santiago, Chile.

Corresponding author address: Maximiliano Viale, Departamento de Geofísica, Universidad de Chile, Blanco Encalada 2002, Santiago, Chile.
E-mail: maxi@dgf.uchile.cl

Doppler radar observations in the Coastal Observations and Simulations with Topography experiment (COAST; Bond et al. 1997) identified the mesoscale evolution and modification of landfalling frontal systems. Using these data, Colle et al. (1999) documented the modification and splitting of a cold front approaching and moving around the Olympics Mountains. Yu and Smull (2000) analyzed the blocking effect on low-level flow leading to the rapid genesis of a narrow cold-frontal rainband (NCFR) in the vicinity of a front approaching the coast. They noted similarities between the blocking-induced frontal evolution and the current gravity theory of squall lines (Rotunno et al. 1988). Later, Colle et al. (2002) extended the Yu and Smull study using a high-resolution simulation to determine the role of the coastal orography, the synoptic-scale dynamics, and the diabatic contributions to the rapid intensification of the NCFR.

The kinematic and microphysical substructure of the NCFR and other mesoscale rainbands has been characterized during the Cyclonic Extratropical Storm (CYCLES) Project offshore of Washington State, before being altered by the coastal and Olympic Mountains. Based on airborne radar observations, CYCLES papers have associated the NCFR with the highest precipitation rates within the frontal systems approaching the coast. The NCFR is organized in a series of small precipitation maxima (cores) along the surface front and interrupted by depressed precipitation rate regions (gaps) between them (e.g., Hobbs and Biswas 1979; Matejka et al. 1980; Hobbs and Persson 1982). Field measurements and modeling studies from CYCLES have further suggested that seeder-feeder mechanisms increase precipitation from mesoscale rainbands (Matejka et al. 1980; Hobbs and Persson 1982; Rutledge and Hobbs 1983). The proposed dominant mechanism for intense precipitation in the NCFR has been associated with graupel that grows rapidly by the riming of ice particles entering the NCFR from stratiform clouds ahead of the front (Rutledge and Hobbs 1984). However, the convective and microphysical processes in the CYCLES Project have not been connected with orographic precipitation enhancement.

While previous studies have noted an association of the blocking effect on low-level flow with upstream enhancement of precipitation and the frontal precipitation (e.g., Doyle 1997; Colle et al. 2002; Neiman et al. 2008; see also the review by Houze 2012), the physical processes contributing to the orographic enhancement of precipitation upstream of a high mountain range, such as the Andes, have not previously been determined. Our purpose is to identify the physical mechanism(s) by which orography contributes to the precipitation enhancement over and upstream of the Andes when that mountain range is approached by a frontal system with

an atmospheric river. The high-altitude and distinct meridional orientation of the Andes together with the well-defined nature of frontal systems moving into South America from the Pacific Ocean make the region of this study an excellent natural laboratory for determining such processes. We examine here a case of an intense cold front and associated NCFR moving eastward and equatorward across the Andes. We employ a high-resolution simulation and complementary surface observations, soundings, satellite infrared images, and the Tropical Rainfall Measuring Mission (TRMM) Precipitation Radar (PR) data. The selected case study occurred on 7–8 June 2006, and produced large precipitation rates over central Chile and the Andes, which caused flooding and damage in the region. The city of Santiago, Chile, received 58 mm of precipitation from 0000–1200 UTC 8 June 2006 with the passage of the front and the NCFR. This amount of precipitation in half a day is equivalent to $\sim 20\%$ of the total annual mean precipitation and demonstrates the importance of understanding these events in the Andean region.

2. Data and model description

Surface weather stations at Pudahuel (PUD) and Concepción (CON), and the rawinsonde station at Santo Domingo (SDM) on the Pacific coast from the Dirección Meteorológica de Chile (DMC) were used (Fig. 1a). The rawinsonde provides data at 0000 and 1200 UTC. TRMM provided data at 1157 UTC 7 June 2006 (the only useful swath during the storm time), concurrent with the sounding, the TRMM data product 2A25, which includes the three-dimensional field of attenuation corrected reflectivity from the TRMM PR (Iguchi et al. 2000a,b). We also used meteorological data from the National Centers for Environmental Prediction (NCEP) Climate Forecast System Reanalysis (CFSR; Saha et al. 2010) to verify the model's performance off the Pacific coast. The CFSR data are available at a resolution of 0.5° every 6 h from 1979 until the present.

We compensate for the scarcity of observations in the region by using model output from a high-resolution simulation with the Weather Research and Forecasting (WRF) Model, version 3.1 (Skamarock et al. 2008), which is nonhydrostatic and uses a terrain-following vertical coordinate (σ). Three nested domains were configured with 36-, 9-, and 3-km grid spacing (Fig. 1b), and 39 vertical levels vertically stretched and maximized in the boundary layer in all domains. The topography of the inner domain with 3 km of resolution is also shown in the Fig. 1a. The simulations were run for 96 h, from 1200 UTC 5 June to 1200 UTC 9 June 2006. Initialization and updated boundary conditions every 6 h were provided

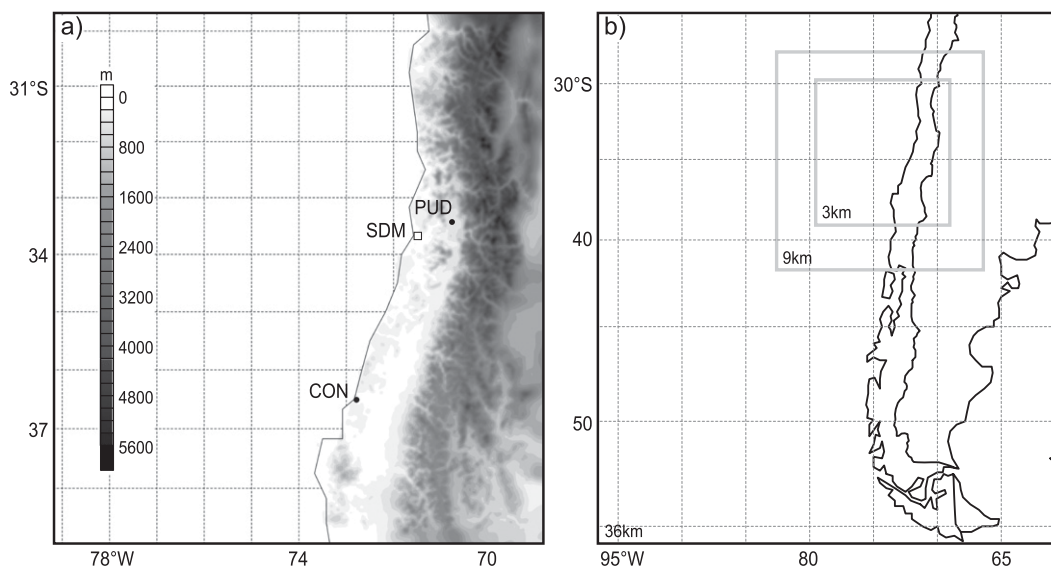


FIG. 1. (a) Topographic map of the inner domain shaded in meters. The white square and black circles indicate the locations of the Santo Domingo (SDM) rawinsonde station, and the Concepcion (CON) and Pudahuel (PUD) surface stations, respectively. (b) Nested domains in the WRF Model using 36-, 9-, and 3-km grid spacing.

from the NCEP Final Analyses (FNL) Global Forecast System (GFS) with $1^\circ \times 1^\circ$ latitude–longitude horizontal resolution.

The physical parameterizations selected in the WRF simulations are listed in Table 1. In particular, the latest available Thompson microphysical scheme (Thompson et al. 2008) was used since its snow parameterization has been shown to reasonably simulate wintertime precipitation over the mountainous Colorado region (Liu et al. 2011). The Thompson scheme is a single-moment scheme with the exception of the double-moment cloud ice variable, and predicts the mixing ratio of cloud water, rain, cloud ice, snow, graupel, and the number concentration of cloud ice. The Kain–Fritsch scheme for convective processes in the subgrid scale was applied in domains with 36- and 9-km grid spacing, whereas the convection was resolved explicitly in the 3-km grid. The model run used time steps of 180, 60, and 20 s in one-way

nesting mode, and topography data with horizontal resolution of $10'$, $2'$, and $30''$ for domains 1, 2, and 3, respectively.

3. Synoptic setting

The surface FNL GFS data show a cyclone and occluded frontal system moving over and across the Chilean coast 36–60 h before the front reached the coast (Figs. 2a,b). In the 12 h prior to landfall (Figs. 2c,d), the subtropical anticyclone weakened but the cold air remained dammed along the subtropical coast west of the Andes. Meanwhile, the midlatitude trough strengthened to form a deep cyclone with a strong cyclonic circulation.

The WRF Model with 36-km grid spacing accurately reproduced the position and intensity of the cyclone as the front made landfall at about 0000 UTC 7 June 2006

TABLE 1. Physical parameterizations selected in the WRF simulation.

Physic process	Scheme	Reference
Microphysics	New Thompson scheme (new in version 3.1)	Thompson et al. (2008)
Radiation	Longwave: Rapid Radiative Transfer Model	Mlawer et al. (1997)
	Shortwave: fifth-generation Pennsylvania State University–National Center for Atmospheric Research Mesoscale Model (MM5) Dudhia scheme	Dudhia (1989)
Cumulus convection	Kain–Fritsch	Kain and Fritsch (1993)
Surface layer processes	Similarity theory (MM5)	Paulson (1970)
Surface processes	Noah land surface model with four layers of temperature and soil moisture	Chen and Dudhia (2001)
Boundary layer processes	Yonsei University (YSU) PBL	Hong et al. (2006)

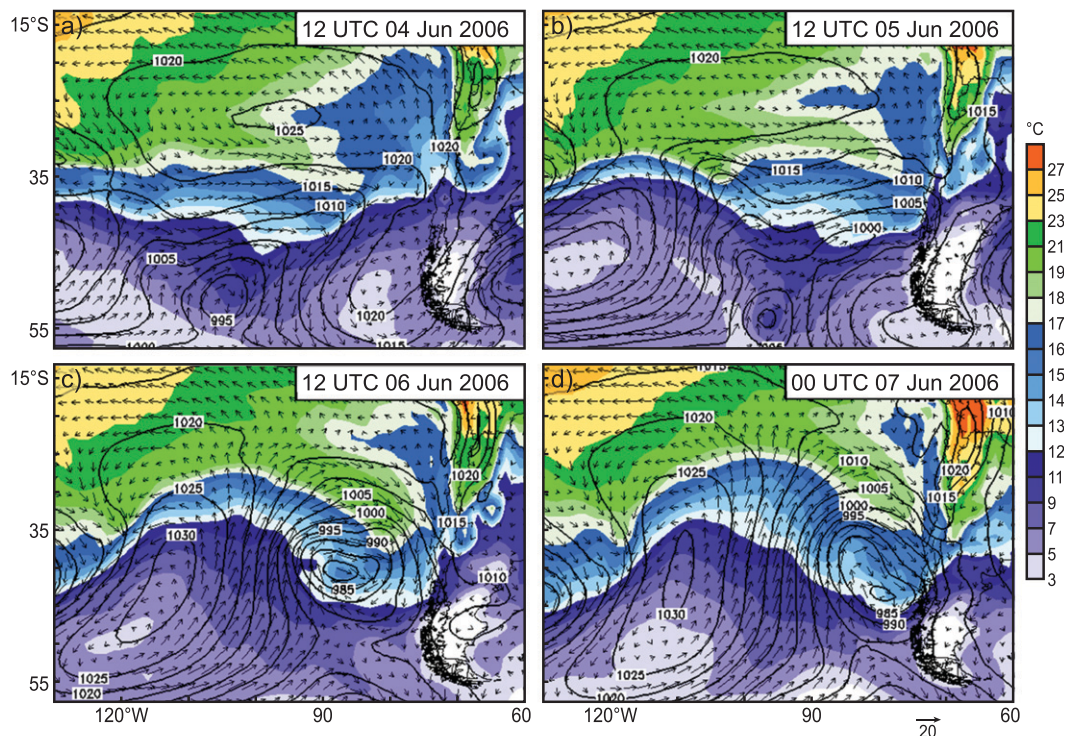


FIG. 2. The NCEP FNL from the GFS showing sea level pressure (solid black contours, every 5 hPa), and winds (arrows, m s^{-1}) and temperature ($^{\circ}\text{C}$, color shaded) at 1000 hPa for (a) 1200 UTC 4 Jun, (b) 1200 UTC 5 Jun, (c) 1200 UTC 6 Jun, and (d) 0000 UTC 7 Jun 2006.

(Fig. 3a). The lowest surface pressure in the center of the cyclone reached a value of 975 hPa at 42° – 43°S , and the near-surface wind shift to the north of its center marked the position of an intense cold front, extending from the ocean to the coast in a northwest–southeast direction (Fig. 3a). As a result, strong low-level northwesterly flow, just ahead of and parallel to the front, advected moisture from the subtropical Pacific Ocean to the coastal region. The WRF simulation results in Fig. 3a also show that the moisture transport was concentrated in a narrow and long corridor of the type known as an “atmospheric river” (e.g., Zhu and Newell 1998; Ralph et al. 2004). Heavy precipitation events over the Andes are often associated with atmospheric rivers (Viale and Nuñez 2011). This atmospheric river comprised the principal source of moisture for the NCFR.

The infrared satellite image depicted an inverted comma cloud pattern associated with the cyclone at 2345 UTC 6 June 2006, with cloudiness inhibited immediately to the lee of the crest of Andes (indicated approximately by the Argentina–Chile border in Fig. 3b). The colder cloud tops just upstream of the crest of the Andes suggests an orographic enhancement of mid and upper-level cloudiness (interior of the red square in Fig. 3b).

4. Mesoscale description of the cold front and comparison with TRMM data

We present in this section a mesoscale description of the cold front and associated rainbands. Because of the limited observations, we must rely heavily on the WRF simulations, but we will show that the model results are substantially consistent with the CFSR reanalysis data and the available TRMM PR and surface observations.

a. Cold front evolution and upstream enhancement of precipitation

Figure 4 shows the mesoscale evolution of the near-surface cold front and associated wind fields simulated by the WRF Model with 3-km grid spacing. The front was distinguishable near the coast at 2100 UTC 6 June as an arcing line associated with a wind shift tied to a well-defined discontinuity in the potential temperature θ field (~ 2 K in Fig. 4a). Six hours later (Fig. 4b), the front aligned straighter intersecting the coastline and the mountain range at an acute angle, and underwent some disruption upstream of the coast (west of 78°W), suggesting faster equatorward propagation over the open ocean. At 0900 UTC 7 June (Fig. 4c), the angle between the coastline and the front gradually became more

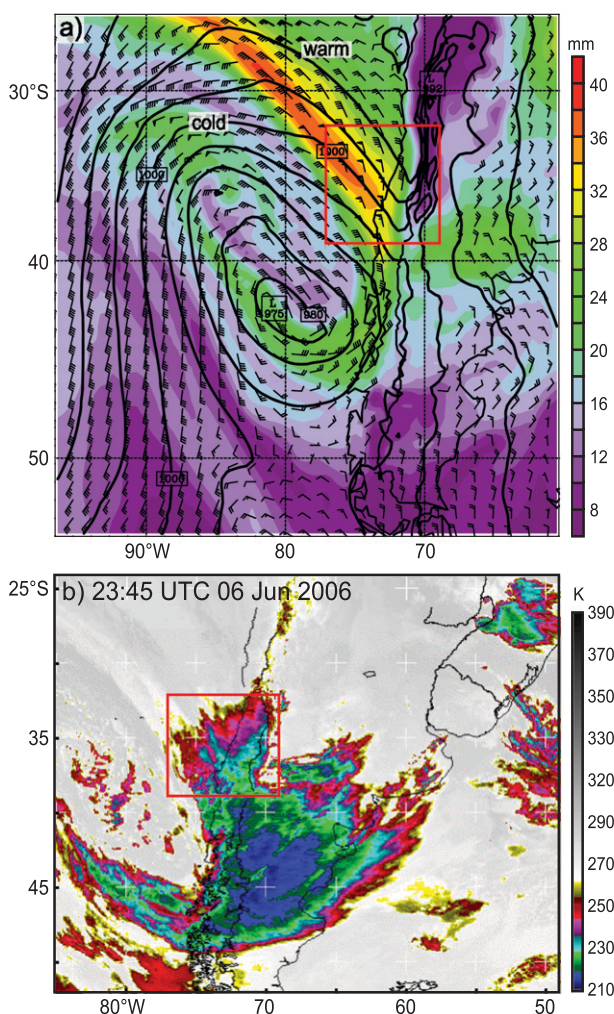


FIG. 3. (a) Surface pressure (black contours, every 5 hPa), 925 hPa-level wind barbs (full barb = 5 m s⁻¹), and precipitable water vapor (shaded every 2 mm from the WRF 36-km run at 0000 UTC 7 Jun 2006). (b) Infrared satellite data showing brightness temperature at 2345 UTC 6 Jun 2006 (shaded in K). The red squares in (a) and (b) enclose the cloudiness top upstream of the Andes and mostly ahead of the surface cold front region.

acute, suggesting a strong disruption of the front by upstream blocking of the low-level flow by the mountains, which slowed down its equatorward progress just upstream of the Andes. This orographic effect on the structure of the frontal system is in agreement with previous case studies of fronts approaching coastal mountain ranges of both Chile and California (Barrett et al. 2009; Doyle 1997; Yu and Smull 2000). Finally, the wind shift zone associated with the well-defined discontinuity in the θ field was not clearly distinguishable at 1500 UTC 7 June (Fig. 4d).

Another feature of the simulated cold front evolution in Figs. 4a–c is the cooling just upstream of the Andes

and ahead of the front, which may be a result of cold-air damming from previous days. The rising air associated with the frontal system must ascend this pooled dense air. Diabatic effects from evaporating and melting precipitation could have produced or contributed to this cooling; light and continuous precipitation was observed and simulated at CON previous to the passage of the front, between 1200 UTC 6 June and 0900 UTC 7 June 2006 (Figs. 6a,c). In a study of upslope flow over the Sierra Nevada in California, Marwitz (1987) noted cooling from such diabatic effects and further suggested that it might strengthen the barrier jet.

Figure 5 shows the simulated 1-h accumulated rainfall field at 6-h intervals associated with the progress of the cold front. The maximum precipitation rates formed a long rainband associated with a confluence of the low-level winds. The band extended from the open ocean to the foothills of the Andes. The change with time of the angle between the rainband and the coastline corresponded to the change of the angle between the front and the coastline. When the cold front made landfall (Fig. 5b), the precipitation field exhibited similarities to the three primary precipitation zones identified by Barrett et al. (2009). These precipitation zones are the Pacific zone, represented by the sector of the rainband located west of 78°W (Fig. 5b); the coastal zone, the sector of the rainband eastward of 78°W to the foot of the Andes; and the windward zone formed in advance of the front over the western slope of the Andes. As in the previous case study of Barrett et al. (2009), the Pacific zone shifted equatorward faster than coastal zone (Fig. 5b); however, the two zones joined farther from the coast in our case study (78°W, ~600 km west of the coast) than in their case study (~50 km west of the coast, see Fig. 5b of Barrett et al. 2009).

As the front moved over the coastline, the portion of the rainband intersecting the coastline moved equatorward (Figs. 5b,c), and the precipitation intensity in the rainband increased toward the coast, closer to the Andes. Over the open ocean, the atmosphere was saturated, the temperature profile was moist adiabatic, and the winds were blowing from the northwest below 400 hPa, just before the passage of the cold front (Fig. 6a). After the passage of the front (Fig. 6b), subsaturated conditions were present and a rotation to westerly winds was noted at low and middle levels (Fig. 6b). The WRF Model aptly reproduced the offshore thermodynamics and dynamics during the pre- and postcold frontal conditions, although some deficiencies could be noted. Drier conditions above (below) 500 hPa and stronger (weaker) near-surface winds were simulated before (after) the passage of the front, as well as a slight deviation in the near-surface wind direction before the passage of the front.

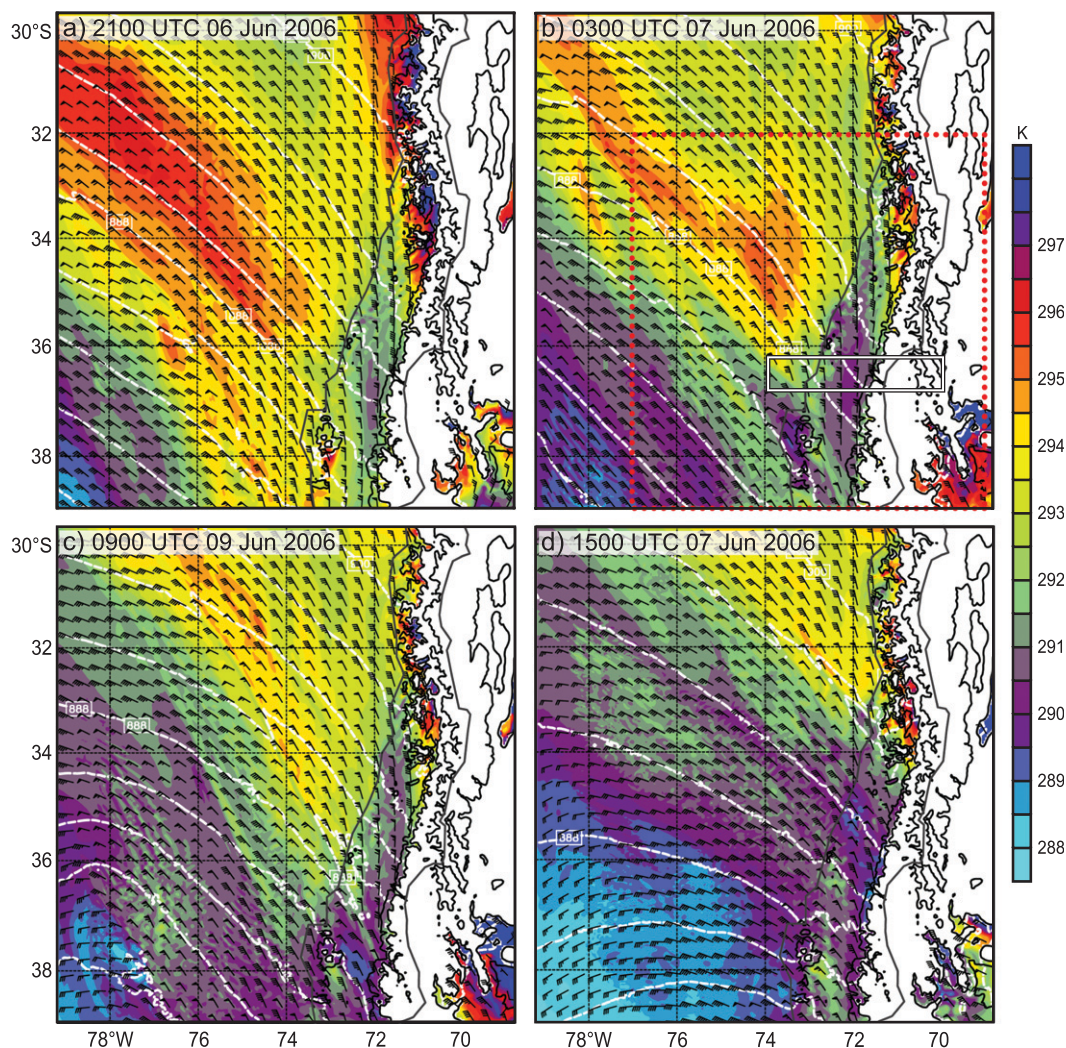


FIG. 4. Potential temperature (color shaded every 1 K) and pressure (dashed white line every 3 hPa) at 1-km vertical level, and wind barbs (full barb = 5 m s^{-1}) at 0.5-km level from the WRF 3-km run at (a) 2100 UTC 6 Jun, (b) 0300 UTC 7 Jun, (d) 0900 UTC 7 Jun, and (d) 1500 UTC 7 Jun 2006. The 500- and 1000-m terrain altitudes are indicated with solid black lines. The outer red-outlined box in (b) covers the same area as the box in Fig. 3. The inner gray box corresponds to the area of the cross-barrier plot in Fig. 11.

Over the continent and upstream of the Andes, surface observations registered a maximum of 1-h rain accumulations first at 0700 UTC 7 June at CON in the south (Fig. 7a) and then at 0400 UTC 8 June 2006 at PUD in the north (Fig. 7b). A sea level pressure (SLP) minimum at CON (Fig. 7a) linked the rain maximum to the passage of the front. Frontal wind shifts were somewhat obscured as a result of the Andes blocking. The WRF 3-km grid simulation accurately captured the timing of the rainband passage at CON and PUD (Figs. 7c,d); however, the magnitude of maximum 1-h precipitation was slightly overestimated, especially at CON (Fig. 7c). The SLP minimum, the temperature, dewpoint temperature, and wind evolution were reproduced well at CON

(Fig. 7c), but with some deficiencies at PUD, where the model produced drying and warmer prefrontal conditions and an unrealistic wind variation (Fig. 7d). These deficiencies at PUD could arise from the complexity of the terrain surrounding the station. CON is located on the coast, while PUD is located in an inner valley between the coastal and the Andes ranges. From these basic comparisons, we conclude that the model successfully reproduced the main mesoscale features of the rainband and general features of the frontal passage, particularly upstream of and over the coast where the low-level flow is minimally altered by the rough terrain of central Chile.

The 36-h total precipitation for the period during which the frontal system was impacting the coast

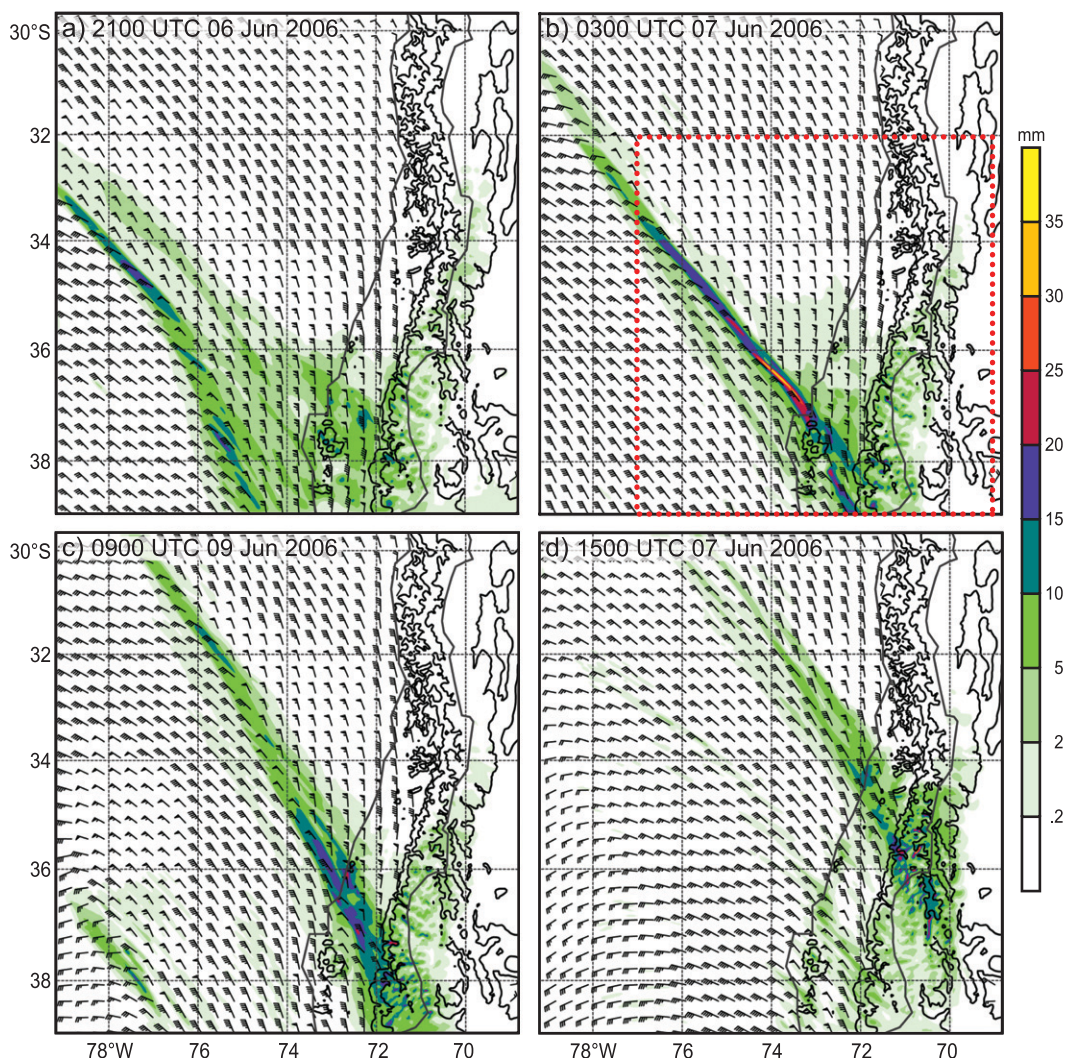


FIG. 5. Winds (full barb = 5 m s^{-1}) at 0.5-km level and 1-h accumulated precipitation (colors) simulated by the WRF 3 km at (a) 2100 UTC 6 Jun, (b) 0300 UTC 7 Jun, (c) 0900 UTC 7 Jun, and (d) 1500 UTC 7 Jun 2006. Solid black lines indicate the 500- and 1000-m terrain altitudes. The red-outlined box in (b) covers the same area as the box in Fig. 3.

between 30° – 39° S highlights how far upstream of the Andes the precipitation was enhanced, particularly over the lowlands of central Chile and offshore over the Pacific Ocean (Fig. 8). The precipitation enhancement was gradually reduced toward the open ocean but nevertheless extended out to around 600 km upstream of the Andes crest, denoting a prominent influence of the cordillera on the upstream precipitation. The Rossby radius, $l_R = NH/f$, (where N is the Brunt–Väisälä frequency, H is the mountain height, and f is the Coriolis parameter) is commonly used to estimate a maximum upstream extent of the terrain influences on the flow (Pierrehumbert and Wyman 1985). Using the sounding at 0000 UTC 8 June 2006 (closer time to the front passage at 33.5° S) and considering the mean altitude of the

32° – 35° S barrier ($H \approx 4000 \text{ m}$), we obtain the saturated Brunt–Väisälä frequency (Durrán and Klemp 1982) $N_m = 1.23 \times 10^{-2} \text{ s}^{-1}$, calculated between successive available levels below 4000 m and then averaged over all sublayers, $f(33.5^{\circ}\text{S}) \approx 8 \times 10^{-5} \text{ s}^{-1}$, and thus $l_R \approx 613 \text{ km}$, which is coherent with the simulated precipitation field.

b. Rainband structures

It can be seen in Fig. 9a that the wind shift zone at 0.5-km level is tied to a narrow and elongated zone of high rainwater content, which strongly suggests that the front near the surface was marked by a NCFR of the type described by Kessler and Wexler (1960), Houze et al. (1976), Hobbs and Biswas (1979), James and

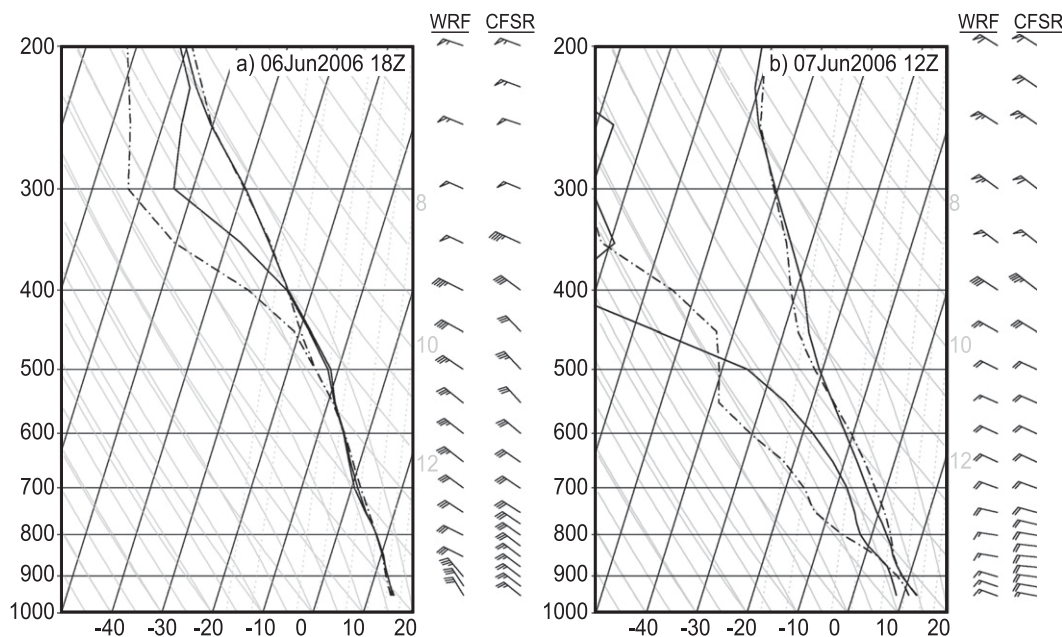


FIG. 6. Skew T -log p diagrams showing the vertical profiles offshore at 34°S and 78°W during (a) precold frontal conditions at 1800 UTC 6 Jun and (b) postfrontal conditions at 1200 UTC 7 Jun 2006. The black solid lines correspond to profiles from reanalysis CFSR data and the dashed-dotted lines correspond to the WRF 3-km output. The profiles show the temperature ($^{\circ}\text{C}$, right line), dewpoint temperature ($^{\circ}\text{C}$, left line), and winds (half barb, 5 m s^{-1} ; full barb, 10 m s^{-1} ; pennant, 50 m s^{-1}).

Browning (1979), Matejka et al. (1980), and Hobbs and Persson (1982). The widespread rainwater content surrounding the simulated front also exhibited several elongated maxima both behind and ahead of the NCFR, suggesting the development of other cold frontal rainbands of the type also described in previous studies (Houze et al. 1976; Matejka et al. 1980; Houze 1993, see chapter 9). The NCFR moves with the surface convergence line of the front, while the other cold frontal rainbands are advected by low- to midtropospheric winds above the surface so that the different rainbands may overtake or cross each other. The overlay in Fig. 9b shows that the TRMM PR definitively verified the existence of the rainbands seen in the model output.

Figure 10 presents vertical sections in the alongfront and cross-front directions, as seen by the TRMM PR and for the WRF 3-km simulation (the position of the profiles are indicated in Fig. 9a). The TRMM PR showed regions with reflectivity maxima extending upward from the surface to about 3 km in the alongfront profile over the wind shift zone (Fig. 10a). The intermittency of the structure is consistent with the precipitation gaps and cores typically seen NCFRs (Hobbs and Biswas 1979; Hobbs and Persson 1982). In the cross-front profile taken from northeast to southwest (left to right in Fig. 10b), the second rainband, which was the NCFR, contained the highest precipitation rates.

The WRF 3-km grid simulation well reproduced the overall structure and position of substructures of the NCFR seen in the TRMM PR data, including the precipitation cores and gap regions of the NCFR in the alongfront profile (Fig. 10c). For example, the wide rainwater mixing ratio maximum with three secondary maximums resembled the structure depicted by TRMM data over the ocean, as well as the increased graupel content on the western slope of the Andes. However, the successive rainwater mixing ratio maximums over the rough coastal terrain are not realistic, since the TRMM data depicted less defined substructures over the coastal terrain (Fig. 10a). In the cross-front profile, the strongest updraft and largest concentrations of rainwater and graupel were simulated in the same position as the highest TRMM PR reflectivity observations (Fig. 10d).

c. Upstream blocking and barrier jet

The Froude number (Fr) is widely used to determine if the cross-barrier component of the wind encountering a mountain range will rise over the barrier or be blocked and flow around the mountain. This number is defined as $Fr = u/hN$, where u is the cross-barrier wind component, N is the dry or moist Brunt-Väisälä frequency, and h is the height of the mountain influencing a given vertical level (distance between the level and the top of the terrain, taken here to be 4000 m). As with the Rossby

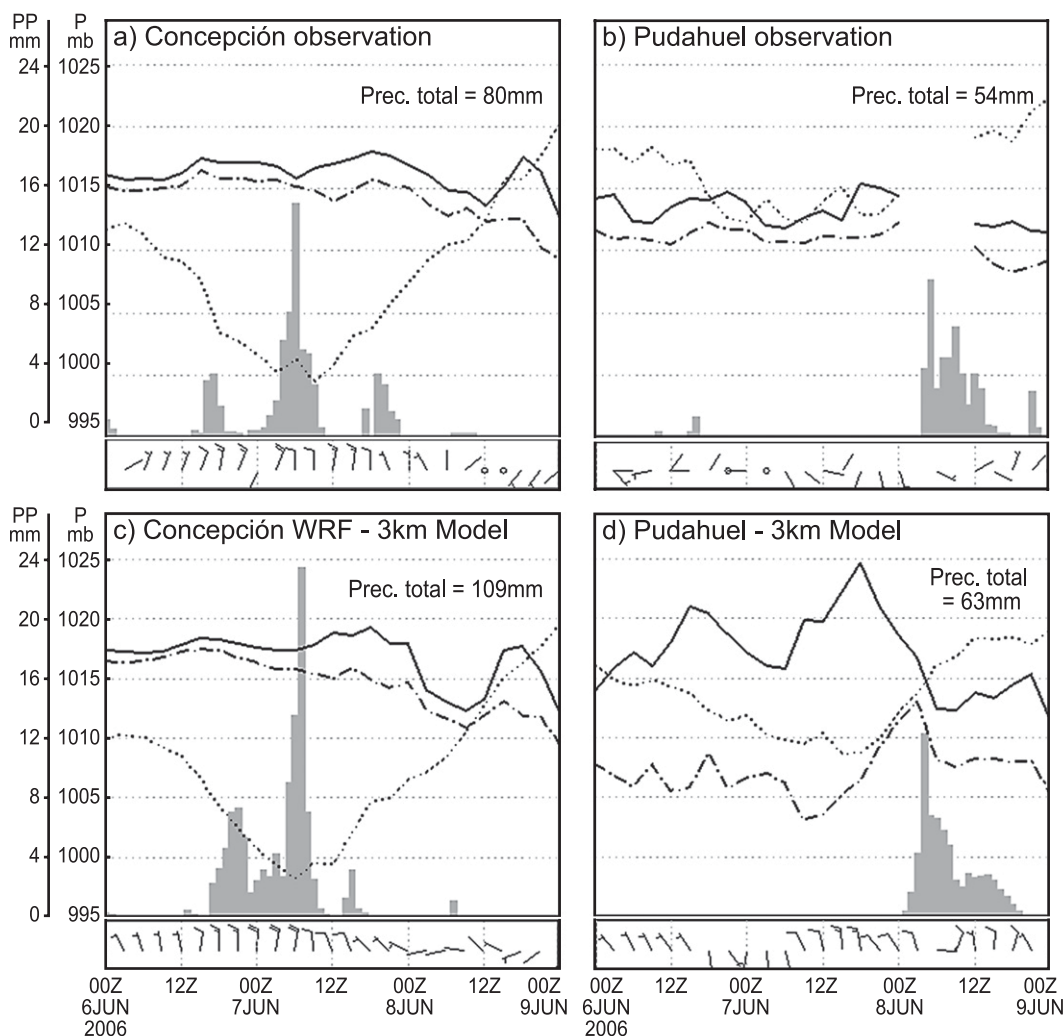


FIG. 7. Meteorgrams for (a) Concepción and (b) Pudahuel (International Airport in Santiago) stations with 3-hourly observations from 0000 UTC 6 Jun to 0000 UTC 9 Jun 2006. Parameters shown are the 2-m temperature ($^{\circ}\text{C}$, black solid line), 2-m dewpoint temperature ($^{\circ}\text{C}$, dot-dashed black line), sea level pressure (mb, black dots), winds (full barb = 10 m s^{-1}), and 1-h precipitation (bars in mm). (c),(d) As in (a),(b), but showing output from the WRF 3-km grid simulation. The locations of both surface stations are shown in Fig. 1a.

radius, N was calculated in all sublayers available below h and then averaged. The sounding data at SDM indicated a blocked or flow-around regime (i.e., $\text{Fr} < 1$) at low levels during and just after frontal passage (Fig. 11). Only parcels above 2500 m were able to surpass the Andes Cordillera around 33.5°S , primarily because of stability and the high altitude of the terrain in this section of the Andes. The model realistically reproduced the blocked low-level flow regime, simulating vertical profiles of Fr similar to the observed profiles (gray lines in Fig. 11).

Upstream of the 36° – 37°S sector of the Andes and just ahead of the cold front, the averaged cross-barrier section of the kinematic fields illustrates features of a

profoundly blocked airflow (Fig. 12). This cross-barrier section was produced by taking a meridional average of the 3-km gridded model output in the 36° – 37°S boxed area in Fig. 4b. The airflow featured a well-defined maximum in along-barrier flow or barrier jet (Fig. 12a), and a strong vertical shear layer in the cross-barrier flow sloping upward from the coast to the upper reaches of the Andes (Fig. 12b). This barrier jet had maximum poleward winds surpassing 30 m s^{-1} on the windward slopes of the Andes and extended down to the coast to a location just ahead of the front (Fig. 12a). The position of the front was denoted by the strong gradient in near-surface poleward winds over the ocean about 50 km west of the coastline (Fig. 12a). At the same time, the

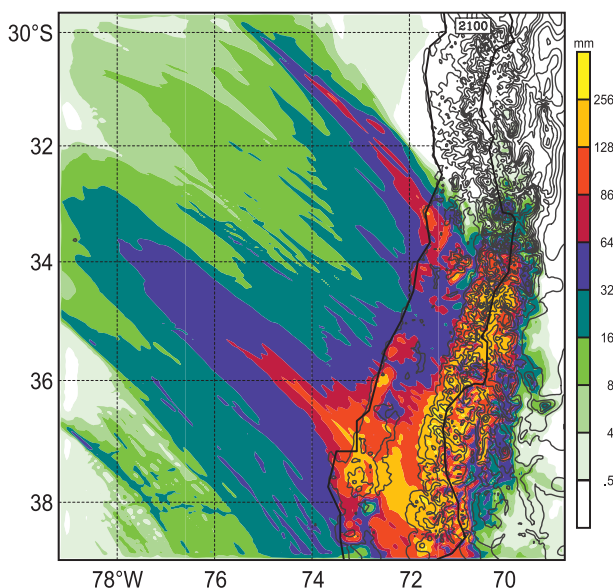


FIG. 8. The 36-h accumulated precipitation field of the WRF 3-km grid simulation, from the 1500 UTC 6 Jun to 2100 UTC 7 Jun 2006. The gray contours show the terrain altitude at 500-m intervals.

low-level cross-barrier flow had a deep layer of weak easterly winds (away from the mountains, i.e., blocked) from the surface to a height of about 1 km upstream of the Andes, except just downstream of the coastal hills where the layer was disrupted by downward and westerly winds (at about 110–130 km on the horizontal scale of Fig. 12b). Above this easterly flow layer, a concentrated layer of cross-barrier wind shear separated the strong westerly flow aloft from the blocked flow below (Fig. 12b). Vertical shear in the cross-barrier wind and the barrier jet have been previously documented as features of orographically blocked airflow upstream of the Andes (Barrett et al. 2009; Viale and Norte 2009), as well as the Sierra Nevada Range (Marwitz 1987), the European Alps (Medina and Houze 2003), and the Cascade Mountains (Medina et al. 2005; Garvert et al. 2007).

Simulated thermodynamic variables are also shown in the cross-barrier sections of Fig. 12. Upstream of the foot of the Andes, the potential temperature θ isolines slope upward slightly while the equivalent potential temperature θ_e contours slope upward with a more pronounced inclination (Fig. 12a). Since the air was near saturation, and the inclination of θ_e was more similar to the upward inclination of the vertical shear in cross-barrier wind and of the barrier jet than that of θ , the isolines of θ_e corresponded to streamlines of the pseudoadiabatic ascent of a steady-state flow over the Andes. This pattern was interrupted by downward-sloping θ lines just downstream of the coastal hills because of dry downslope flow, probably the result of gravity waves in

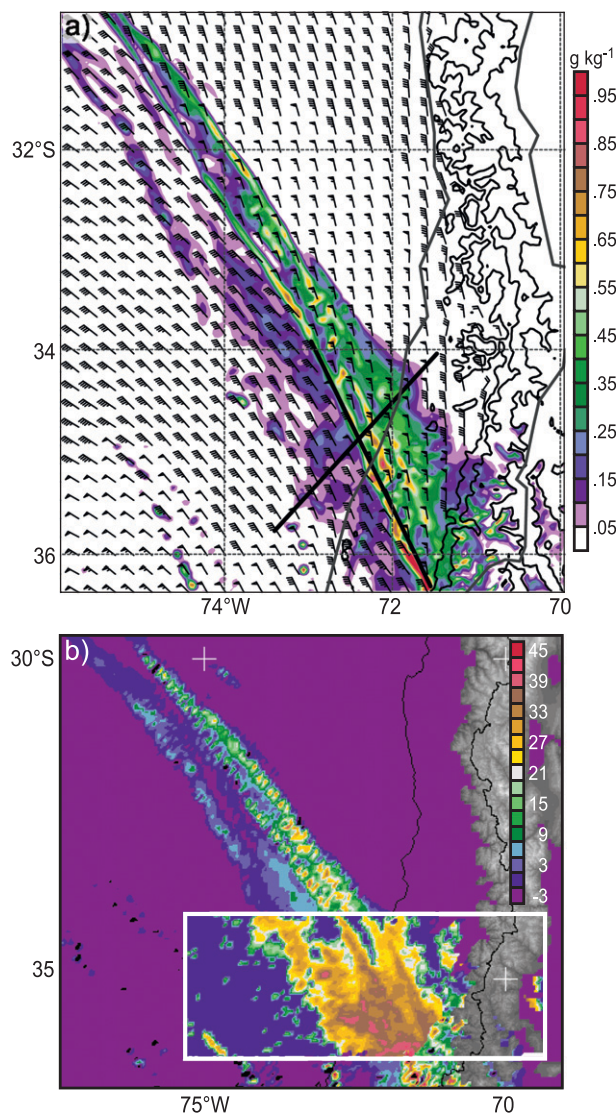


FIG. 9. (a) Winds (full barb = 5 m s^{-1}) at 0.5 km and rainwater mixing ratio at 2 km from the WRF 3-km grid simulation for 1200 UTC 7 Jun 2006. The black lines in the alongfront and cross-front directions correspond to the vertical sections in Fig. 10. (b) Reflectivity from the TRMM PR at 2 km, shaded area in dBZ between white rectangle that bound the satellite swath at 1157 UTC 7 Jun, overlaid on the rainwater mixing ratio (shaded) from the WRF 3-km grid simulation at 2 km at 1200 UTC 7 Jun 2006.

the westerly layer induced by the flow over the low coastal range (Fig. 12a). This local downslope flow produced a local rain shadow (Fig. 8). The 0°C isotherm exhibited a lowering upstream of the main Andes (Fig. 12b), which may have been a result of cold air damming and/or pseudoadiabatic cooling and melting of precipitation. Minder et al. (2011) using idealized simulations have shown that a combination of the latter two mentioned processes contribute to the lowering of the 0°C isotherm upstream of the mountain.

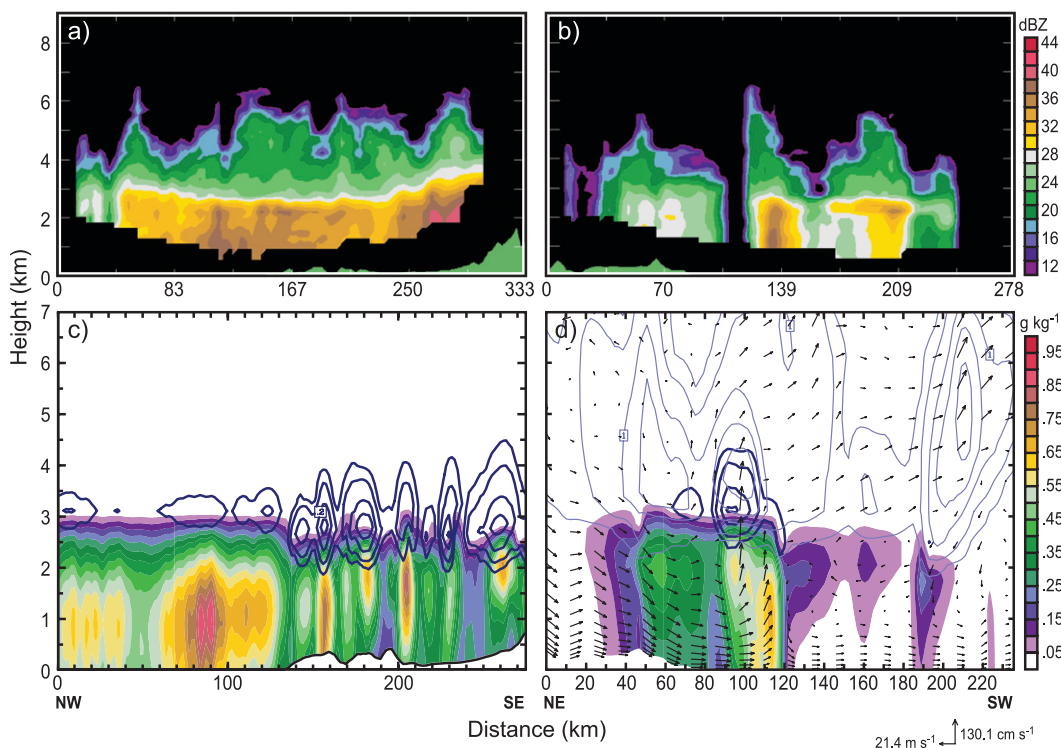


FIG. 10. Vertical sections in (left) alongfront and (right) cross-front directions at 1200 UTC 7 Jun 2006 along the line shown in Fig. 9: (a),(b) TRMM PR reflectivity (dBZ); (c),(d) rainwater mixing ratio (shaded in g kg^{-1}) and the graupel mixing ratio (dark blue contours from 0.05 to 0.2 g kg^{-1}) simulated by the WRF 3-km model. (d) The snow mixing ratios (light blue contour of 0.1, 0.4, 1, and 1.5 g kg^{-1}) and the circulation vectors in the cross-front–height plane (vectors in m s^{-1} in cross-front and in cm s^{-1} in vertical directions). The alongfront and cross-front profiles correspond to the solid black lines in alongfront and cross-front directions indicated in Fig. 9a.

5. Orographic enhancement of precipitation

To gain an understanding of the orographic mechanisms responsible for producing enhanced precipitation from the NCFR in its sector closest to the Andes, we now examine the mesoscale kinematics and microphysical fields in the NCFR and in its surroundings from the WRF 3-km grid simulation, as well as from the sensitivity experiment in which the height of the Andes mountain was reduced.

a. Barrier jet enhancement of the narrow cold frontal rainband

Figure 13 shows the NCFR as an elongated and dominant rainband moving equatorward with the cold front. The simulated rainwater content at the 1-km level exhibited a long and narrow maximum tied to the near-surface wind shift from the ocean to the foot of the Andes in the northwest–southeast direction. The position of the long and narrow maximum of rainwater at each time of Fig. 13 is coincident with the position of the long and narrow maximum of 1-h precipitation accumulations at the same times in Fig. 5. This spatial

coincidence also indicates that the NCFR, situated along the surface cold front, produced the most significant precipitation of the event upstream of the Andes as it moved equatorward.

In addition, Fig. 13 shows that only the sector of the NCFR closest to the Andes was surrounded by snow concentrations higher than 0.1 g kg^{-1} at middle levels, which is consistent with the cloudiness pattern upstream of the mountains shown in the satellite observations in Fig. 3b (enclosed by the square overlaid on Fig. 3b). The simulated shape of the snow hydrometeors surrounding the NCFR in Fig. 13b at the time closest to the satellite observation resembled the cloudiness pattern upstream of the Andes. The enhanced snow content at midlevels ahead of the NCFR and upstream of the mountain suggests that orographic lifting of midlevel flow produced additional ice particles.

Figure 14 shows an alongfront cross section averaged in the cross-front direction in the area of the dashed box B in Fig. 13b. Consistent with 1-h rain accumulations (Fig. 5), the alongfront section of Fig. 14 indicates that the simulated rainwater, graupel, and snow content increased in the rainband, and the 0°C isotherm level

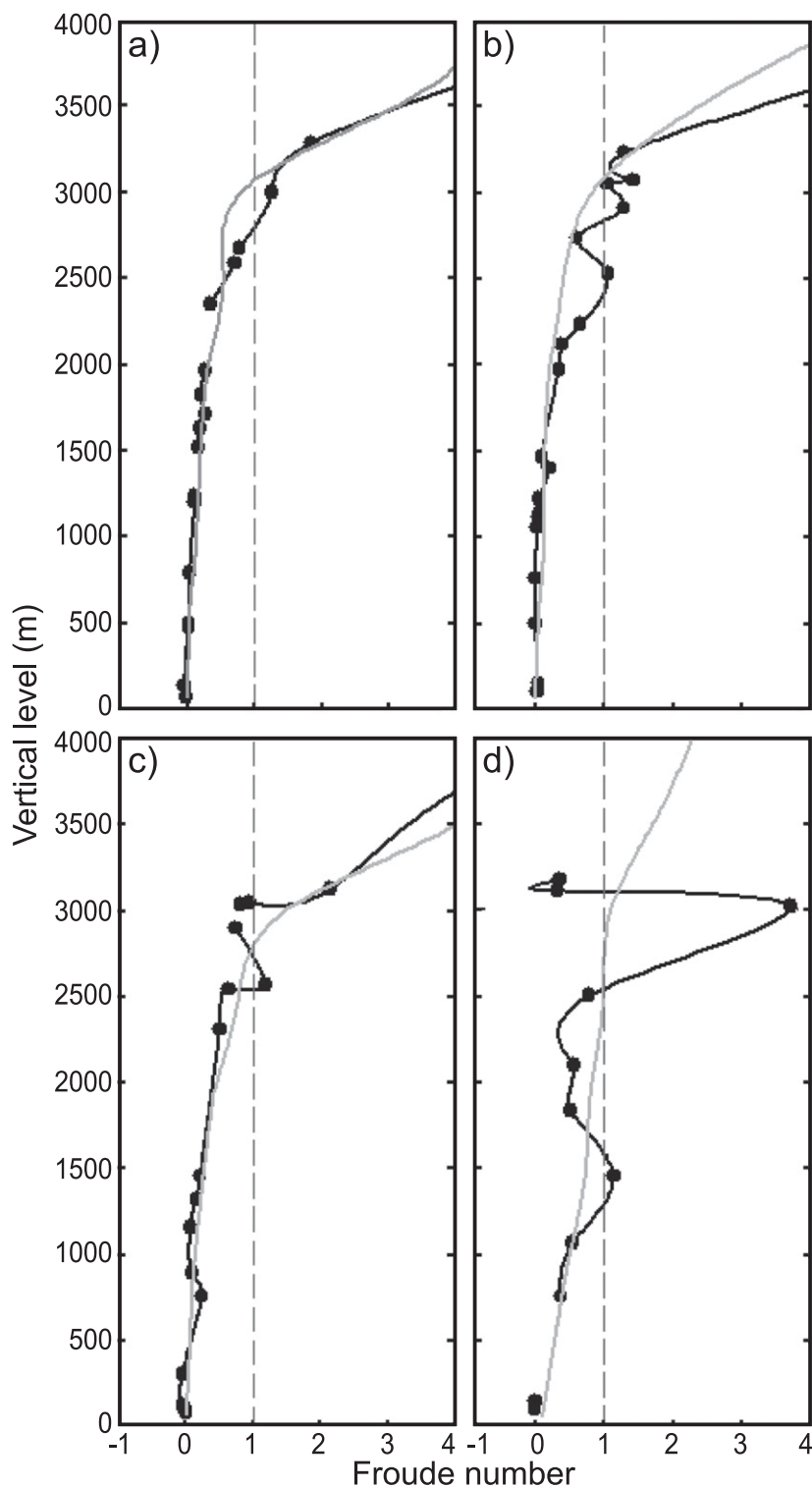


FIG. 11. Vertical profiles of the observed (black line) and simulated (gray line) Froude number at (a) 1200 UTC 6 Jun, (b) 0000 UTC 7 Jun, (c) 1200 UTC 7 Jun, and (d) 0000 UTC 8 Jun 2006. The Froude number, $Fr = u/hN$, was calculated using the Brunt-Väisälä frequency N , and the cross-barrier wind component u from the rawinsonde at SDM on the Pacific coast (Fig. 1a), and the height of the mountain “seen” by each vertical level (h , the distance between the level and the top of the Andes around 33.5°S, which was considered as 4000 m).

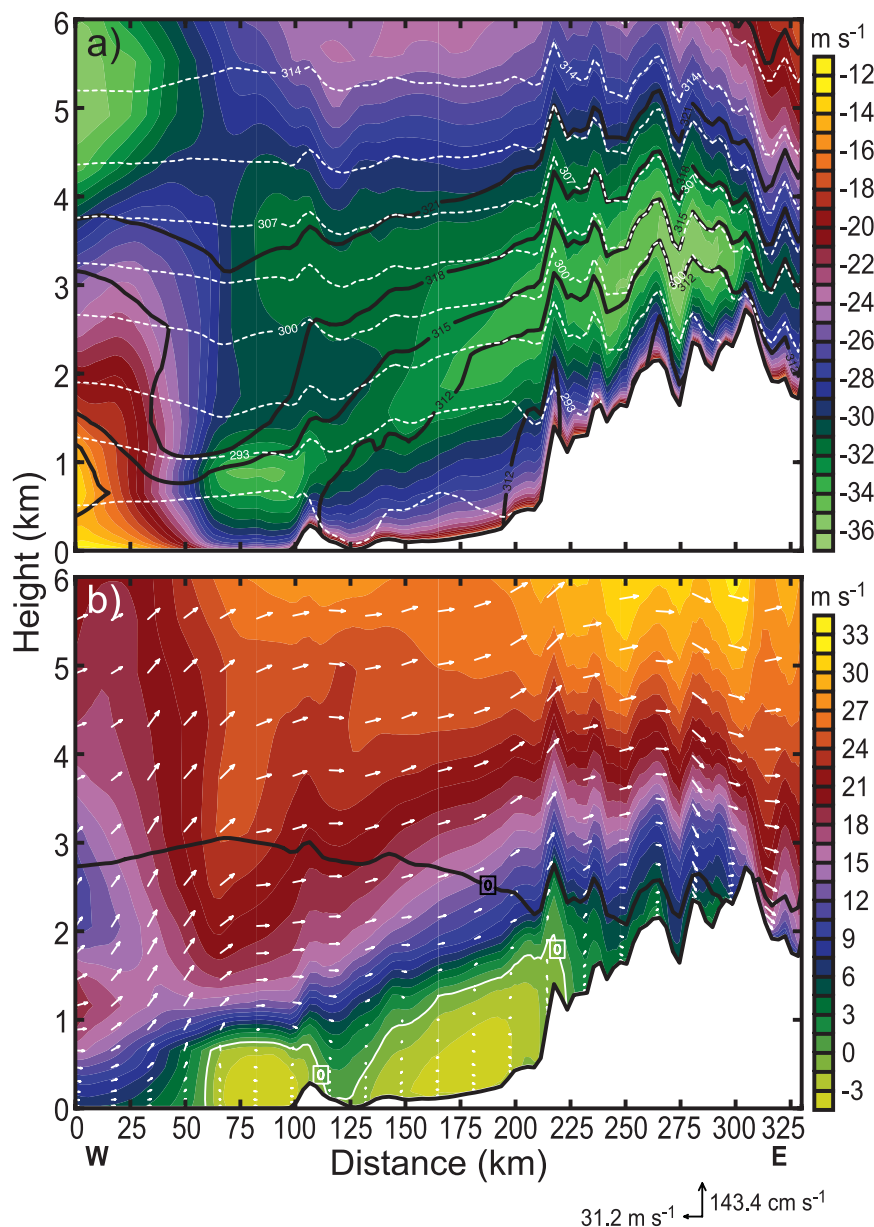


FIG. 12. Meridionally averaged west-east cross section of (a) along-barrier wind (shaded every 1 m s^{-1}), equivalent potential temperature (solid black lines), and potential temperature (dashed white lines); (b) cross-barrier wind (shaded every 1.5 m s^{-1} with the 0 m s^{-1} isoline indicated by the white contour), the 0°C isotherm (thick black line), and the wind in the plane of the cross section from the WRF 3-km grid simulation at 0300 UTC 7 Jun 2006. The west-east cross sections were meridionally averaged in the area enclosed by black lines in Fig. 4b.

lowered, with decreasing distance from the Andean foothills. The 0°C level was about 500 m lower over the foothills than over the open ocean, while the rainwater and snow content in the NCFR increased by factors of 3 and 4–5, respectively, as the distance to the foothills decreased from 600–800 to 100–300 km (Fig. 14). Moreover, graupel content higher than 0.1 g kg^{-1} was simulated at distances $< \sim 600 \text{ km}$ from the foothills.

Figure 15 presents three average cross-front sections, averaged in the alongfront direction in the area of boxes 1, 2, and 3 in Fig. 13b. Zone 1 is farthest from the Andes ($\sim 700 \text{ km}$), zone 2 is at an intermediate distance from the Andes ($\sim 500 \text{ km}$), and zone 3 is closest to the mountain range ($\sim 250 \text{ km}$). A notable increase in the mixing ratios of rainwater, graupel, and snow, as well as in the updraft and in near-surface winds toward the NCFR is apparent

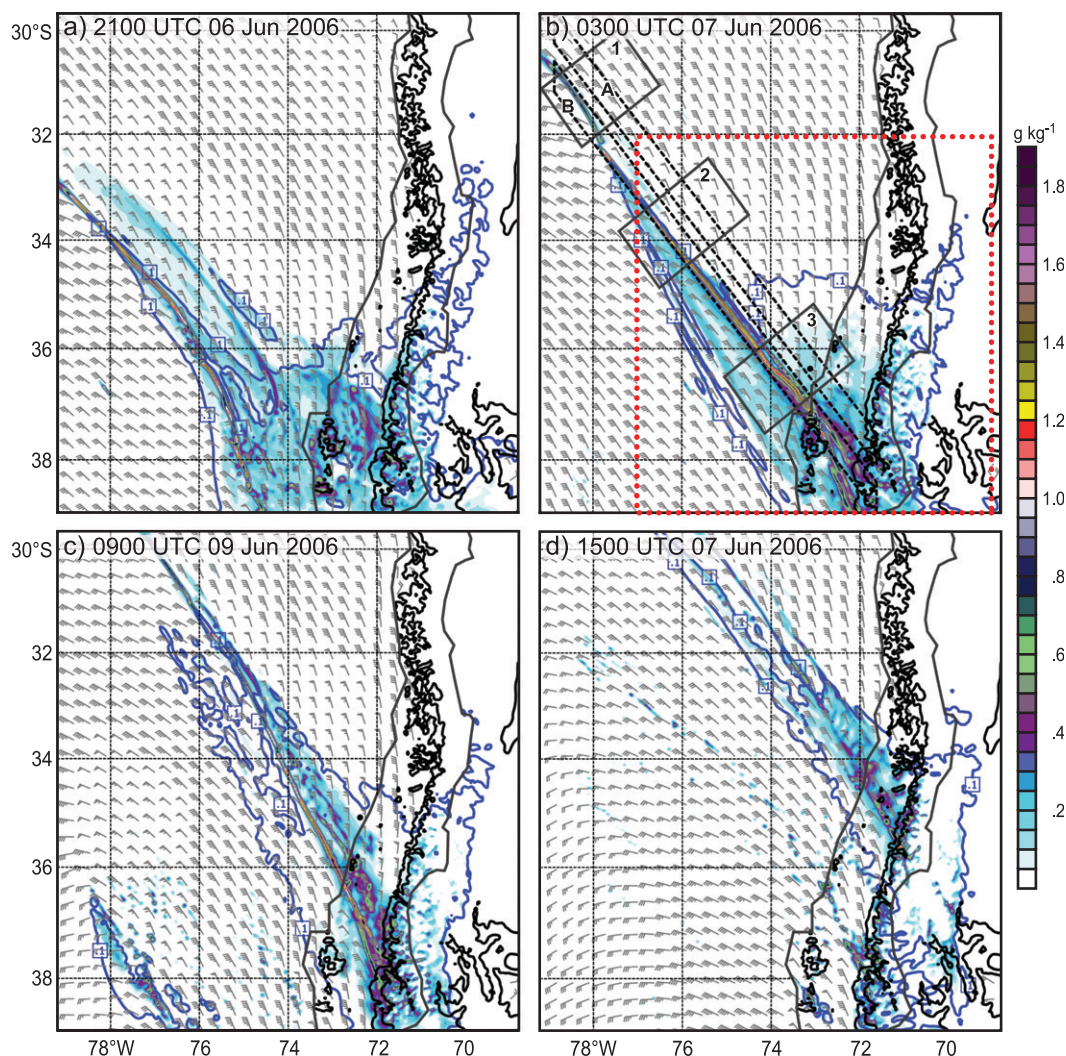


FIG. 13. Winds (full barb = 5 m s^{-1}) at the 0.5-km level, rainwater mixing ratio (shaded in g kg^{-1}) at 1-km level, and the 0.1 g kg^{-1} contour of snow mixing ratio at 3-km level (blue solid line) from the WRF 3-km grid simulation at (a) 2100 UTC 6 Jun, (b) 0300 UTC 7 Jun, (c) 0900 UTC 7 Jun, and (d) 1500 UTC 7 Jun 2006. The 500- and 1000-m terrain contours are in solid black. The solid 1, 2, and 3 boxes in (b) correspond to the area of the cross-front plots in Fig. 15, while the dashed B and A boxes correspond to the area of the alongfront plots in Figs. 14 and 16, respectively. The black circles plotted just ahead of the front on the coast in (b) and (c) correspond to the trajectories end points of Fig. 17.

with decreasing distance from the mountain barrier. The winds were mostly in same direction as the frontal progress in zone 1 (i.e., from southwest to northeast), except for the near-surface layer ahead of the front with weak winds in the opposite direction toward the NCFR (Fig. 15a). Instead, the winds in same direction as the frontal progress above the 1-km level and ahead of the front were reduced in zone 2 (Fig. 15b), and changed to the opposite direction of the front progress in zone 3 (Fig. 15c). The near-surface winds toward the NCFR below 1 km were increased considerably from zone 1 to zone 3 as a result of the upstream blocking and barrier

jet development. The barrier jet, located in the near-surface layer over the ocean, evidently produced an increase in the near-surface convergence and updraft at the location of the surface front and NCFR, which in turn led to larger production of hydrometeors in this sector of the NCFR in the region closest to the Andes.

The simulated mixing ratios of different hydrometeors in the updraft region of the NCFR were highest in zone 3, and higher in zone 2 relative to zone 1 (Fig. 15). While insignificant mixing ratios of graupel and snow were localized just over the weak updraft of NCFR in zone 1 (Fig. 15a), high mixing ratios of graupel and snow

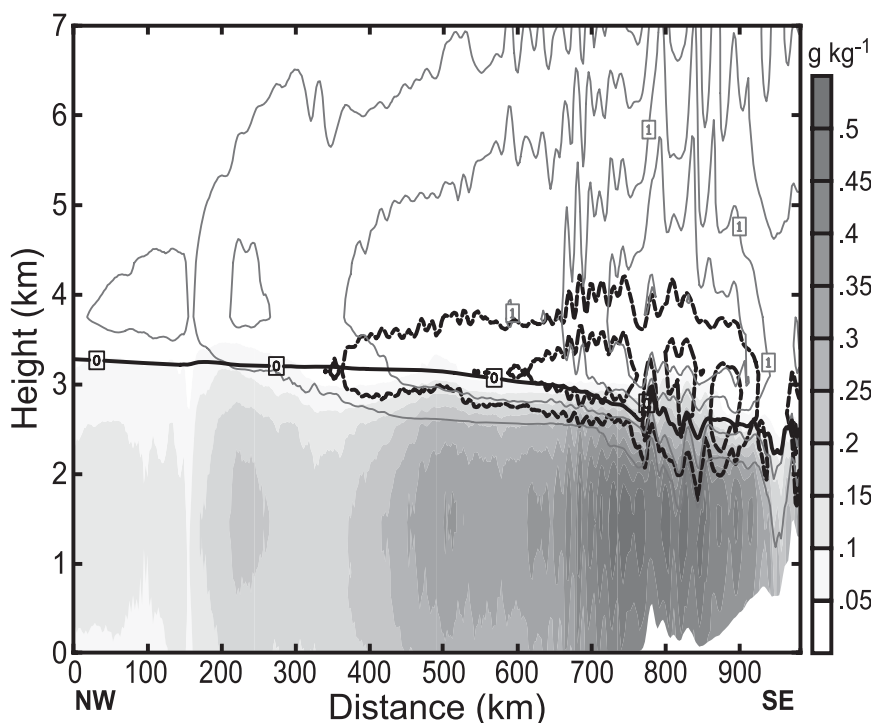


FIG. 14. Average alongfront section (averaged in the area of box B in Fig. 13b) showing the rainwater (shaded in g kg^{-1}), graupel (black lines), and snow (gray lines) mixing ratios, and the 0°C isotherm (thick black line) simulated by the WRF 3 km at 0300 UTC 7 Jun 2006. The graupel and snow contours correspond to 0.05 and 0.1 g kg^{-1} and to 0.1, 0.4, 1, and 1.5 g kg^{-1} , respectively.

were produced above 2.5 km in the strong updraft of the NCFR in zones 2 and 3. Some of the highly concentrated hydrometeors were being advected toward the rear sector of the frontal zone by weak midlevel winds toward the front (Figs. 15b,c). The cross-front section of zone 3 was the only one that had midlevel snow content well ahead of the NCFR, which would be available to interact with liquid water content associated with the strongest updraft of the NCFR and thus contribute to producing a high mixing ratio of graupel by riming (Fig. 15c).

b. Feeder-seeder enhancement of the narrow-cold frontal rainband

To explore the physical process of orographic enhancement of the precipitation ahead of the NCFR and upstream of the Andes, an average alongfront section centered approximately 90 km ahead of the front is presented in Fig. 16, where the averages are taken in the cross-front direction in the area of dashed box A of Fig. 13b. The midlevel circulation vectors in the alongfront direction exhibited an upward component beginning at around 450 km upstream of the foot of the Andes and increased with decreasing distance from the Andes. Consistent with this circulation, the simulated snow

content above the 0°C isotherm started around 500 km upstream of the barrier, with values $>0.1 \text{ g kg}^{-1}$, and sharply increased to 1 g kg^{-1} just upstream of the foothills (Fig. 16). Low-level vertical motion alternated between downward and weak upward motion just upstream of the barrier, while rain mixing ratios $>0.05 \text{ g kg}^{-1}$ begin around 300 km west of the foothills and increased to 0.3 g kg^{-1} just upstream of the foothills. Unlike the alongfront section in the NCFR (Fig. 14), there was no graupel production ahead of the front, which suggests that the low-level updrafts were not strong enough to produce the large amounts of cloud water and rain necessary to generate graupel by riming in addition to having less available water vapor (Figs. 21d and 22e). This also suggests that the light rain in the simulation (Fig. 5) and the observations (Figs. 7a,b) just ahead of the NCFR upstream of the Andes was likely produced by melting snow generated at midlevels.

Trajectories computed from the 3-km gridded model simulation confirm that the midlevel flow ahead of the front rose well upstream of the crest of the Andes, producing a zone of increased concentrations of precipitating ice particles just ahead of the NCFR and upstream of the Andes (Fig. 17). The trajectories were calculated in

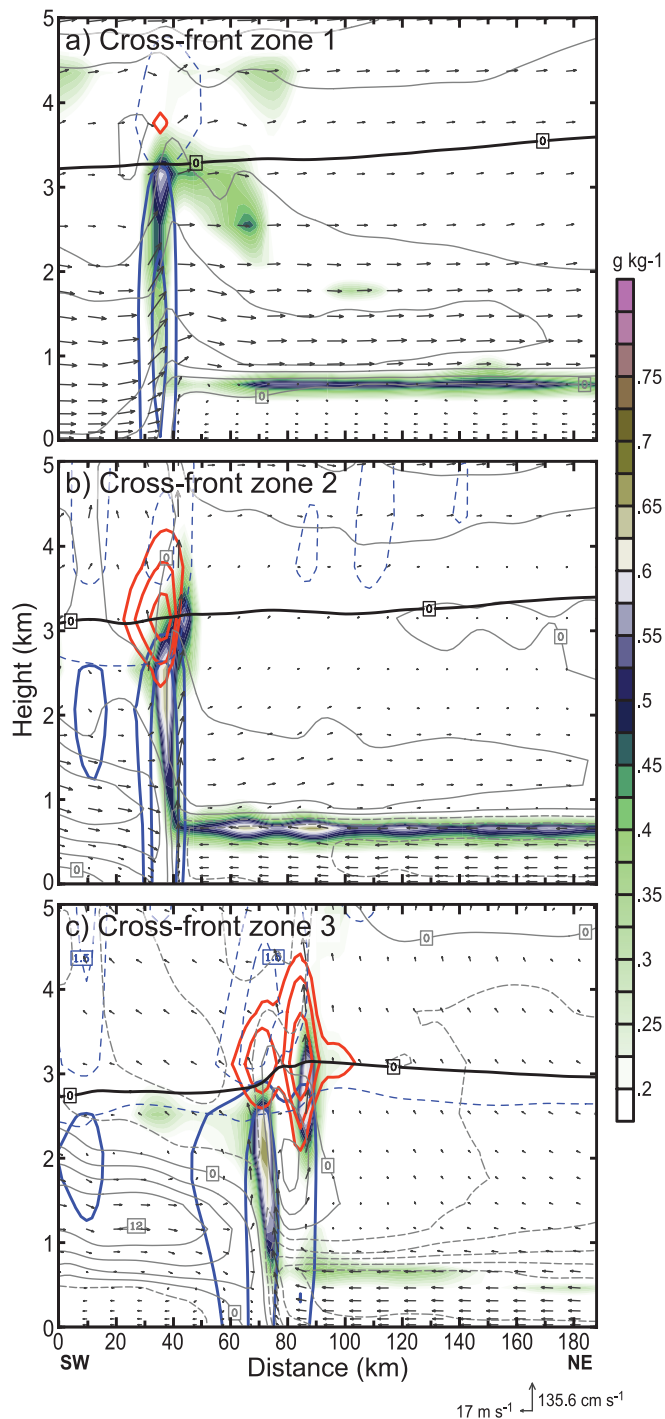


FIG. 15. Average cross-front sections (averaged in the area of boxes 1, 2, and 3, respectively, in Fig. 13b) showing the 3-km resolution simulated cloud water (shaded in g kg^{-1}), graupel (red lines), and snow (dashed light blue lines) mixing ratios, the 0.2 and 0.5 g kg^{-1} contours of rainwater (solid blue lines), the horizontal airflow in cross-front direction (contours every 3 m s^{-1} , positive values are from southwest to northwest and plotted using gray solid lines, the negative values being shown by gray dashed lines), and the circulation wind vector (in m s^{-1} in cross-front and in cm s^{-1} in vertical directions). The 0°C isotherm is also plotted in all panels using a thick black line.

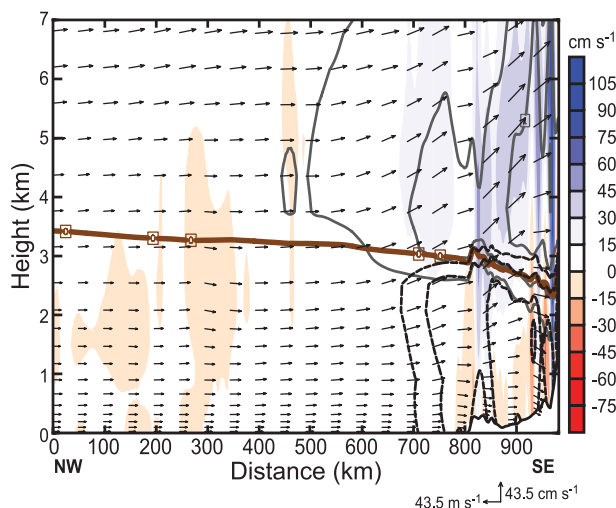


FIG. 16. As in Fig. 14, but for the average alongfront section approximately centered 90 km ahead of the cold front (averaged in cross-front direction in the area of box A in Fig. 13b). The circulation wind vectors in alongfront–height plane simulated by the WRF 3-km grid are added (in m s^{-1} in alongfront and in cm s^{-1} in vertical directions, respectively). The magnitude of vertical component of wind is also shaded every 15 cm s^{-1} . The rain (black dashed line) and snow (gray line) mixing ratio contours correspond to 0.05, 0.1, and 0.3 g kg^{-1} and to 0.1, 0.4, and 1 g kg^{-1} , respectively. The 0°C isotherm is plotted using the solid brown line.

a backward direction using the starting point 1 at the 1-, 2-, 3-, and 4-km levels, for 8 h leading up to 0300 UTC 7 June, and using the starting point 2 at same levels for the 8 h leading up to 0900 UTC 7 June. Both starting points were selected because they were located just ahead of the front and of the NCFR on the coast (see black circles in Figs. 13b,c). The plan-view plot in Fig. 17a reaffirms the displacement of the ahead-of-front parcels in the front-parallel direction, from northwest to southeast, and points out the upstream blocking and poleward deviation of the low-level flow as parcels approach the Andes. The trajectories projected onto the alongfront height plane that reached point 1 (Fig. 17b) show that the lowest parcel (at 1 km) did not rise significantly as it approached the Andes but rather was diverted generally poleward (Fig. 17a). The higher parcels at middle levels rose about 500 m, mostly during the last 1-h time step when progressing from ~ 350 to ~ 260 km in front of the Andes crest at the point 1. The parcels that reached point 2 at 0900 UTC 7 June displayed a very similar evolution (not shown). Consistent with this parcel's evolution, the time series of snow and rain mixing ratio for trajectories shown in Fig. 17b reveal that the ahead-of-front air parcels did not have precipitating hydrometeors as they moved over the open ocean but rather incorporated greater snow content at middle levels than rain content at low levels beginning 1

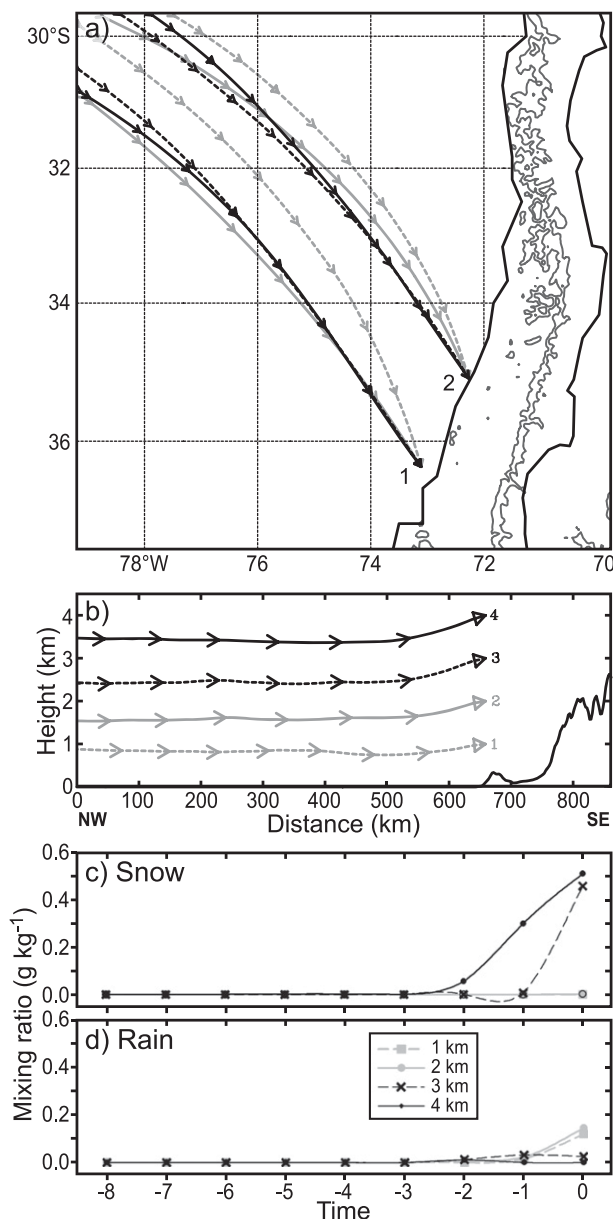


FIG. 17. (a) Map of backward trajectories ending ahead of the cold front at four different heights, 1 km (gray dashed lines), 2 km (gray solid lines), 3 km (black dashed lines), and 4 km (black solid lines), at point 1 at 0300 UTC 7 Jun, and at point 2 at 0900 UTC 7 Jun 2006 (see also black points in Figs. 13b,c, respectively). (b) Trajectories ending at point 1 at 0300 UTC 7 Jun 2006 projected onto the alongfront–height plane from northwest–southeast. (c),(d) Time series of snow and rain mixing ratios for trajectories shown in (b).

or 2 h before reaching point 1 on the coast (Figs. 17c,d). Graupel was only produced during trajectories at the 3- and 4-km levels starting 1 h before reaching point 1, but with very low maximum values of 0.03 and 0.002 g kg^{-1} , respectively (not shown in Fig. 17 since these values are

one and two orders of magnitude lower than the snow and rain content).

The trajectory analysis thus shows that light precipitation ahead of the front was primarily a result of midlevel orographic lifting upstream of the Andes. We infer from this result that the precipitating snow particles ahead of the front play an important role in increasing the upstream precipitation enhancement when they interact with the strong updrafts of the NCFR.

The snow particles of the orographic stratiform cloud accreted the supercooled water of the active updrafts to produce rimed particles, which melted and fell out as enhanced rain. We suggest that this combination of events was the primary physical mechanism by which the orographic precipitation enhancement upstream of the Andes occurred.

c. The reduced Andes simulation (RANDES)

The results presented thus far suggest that the enhancement of the NCFR upstream of the Andes was produced by a combination of low- and midlevel orographic processes: increased low-level convergence in the vicinity of the cold front and a seeder-feeder effect produced by the orographic ascent of midlevel flow just ahead of the front. To quantify the role of these orographic processes on the precipitation from the front and the NCFR, we performed a sensitivity test in which the height of the Andes terrain was reduced 50% everywhere, referred to as the reduced Andes simulation (RANDES), but maintaining identical model configuration to that in the control (CTL) simulation. This amount of reduction makes the mountain range in the RANDES simulation like the lower altitude west coastal mountain ranges of North America (e.g., the Cascade Mountains of Oregon).

The RANDES simulation produced 1-h accumulated rainfall fields (Fig. 18) similar to those in the CTL run (Fig. 5), except that after the cold front made landfall, its equatorward progress was faster than in the CTL, especially its sector closer to the Andes. As the front progressed, it changed to a slightly less oblique angle (between the front and the coastline) in the RANDES simulation (Figs. 18b–d) compared to that in the CTL (c.f., Figs. 5b–d). To quantify the speed of the front as it approached the mountain and moved equatorward, we estimated its speed at the 0.5-km level for both simulations using the two lower points of a moving box along the front. One point is over the ocean and the other point is on the foot of the Andes (see dashed orange moving boxes in Figs. 18b,c, which we also used to calculate different quantities shown later). From 0000 UTC 7 June to 1200 UTC 7 June, the front moved equatorward at 34.5 km h^{-1} over the ocean and at 25.2 km h^{-1}

at the foot of the Andes for the CTL simulation; whereas the front moved at 33.6 km h^{-1} on the ocean and at 33.4 km h^{-1} at the foot of the Andes for the RANDES simulation. The main difference in the speed of the front at the foot of the Andes is coherent with a reduced upstream blocking effect in the RANDES simulation compared to CTL.

Figure 19 quantifies the differences in total accumulated rainfall as the front approached the Andes and crossed the entire region for the RANDES and CTL simulations. Over the upstream of the Andes region (i.e., the area enclosed by dashed lines in Fig. 19), the mean 48-h precipitation was some 25% greater for the CTL than the RANDES simulation. The extreme height of the Andes terrain thus produces an enhanced upstream blocking effect compared to west coastal mountains in North America (as represented by the RANDES simulation), which slows the equatorward movement of the frontal region. As a result, the time that the enhanced precipitation processes can occur increases and more precipitation accumulates in the coastal and upstream ocean regions.

To demonstrate the low-level upstream blocking effect of the Andes on the precipitation, we evaluate the magnitude of the convergence and the Miller Frontogenesis equation (MF; Miller 1948) along the front using the 3-km model output from both simulations. The simplified form of the MF equation solves various terms that can change the magnitude of the horizontal gradient of the potential temperature following the air parcel:

$$\begin{aligned} \frac{d}{dt} |\nabla_h \theta| = \frac{-1}{|\nabla_h \theta|} \left\{ \left[\left(\frac{\partial \theta}{\partial x} \right)^2 \left(\frac{\partial u}{\partial x} \right) + \left(\frac{\partial \theta}{\partial y} \right)^2 \left(\frac{\partial v}{\partial y} \right) \right] \right. \\ + \left[\frac{\partial \theta}{\partial x} \frac{\partial \theta}{\partial y} \left(\frac{\partial v}{\partial x} + \frac{\partial u}{\partial y} \right) \right] + \left[\frac{\partial \theta}{\partial z} \left(\frac{\partial w}{\partial x} \frac{\partial \theta}{\partial x} + \frac{\partial w}{\partial y} \frac{\partial \theta}{\partial y} \right) \right] \\ \left. - \left[\frac{\partial \theta}{\partial x} \frac{\partial}{\partial x} \left(\frac{d\theta}{dt} \right) + \frac{\partial \theta}{\partial y} \frac{\partial}{\partial y} \left(\frac{d\theta}{dt} \right) \right] \right\}. \quad (1) \end{aligned}$$

In (1), the four terms on the right-hand side are stretching deformation (A), shearing deformation (B), tilting (C), and diabatic effects (D). The diabatic term is limited to condensational heating, and does not include cooling from evaporation, sublimation, or melting, and depositional heating. For every 1-h time interval of the model data, each term of the MF equation and the convergence were averaged within a moving box of 20×160 grid points ($60 \times 480 \text{ km}^2$) in the horizontal and lowest eight model vertical levels (an approximately 1200-m layer above the surface). The box moved following the

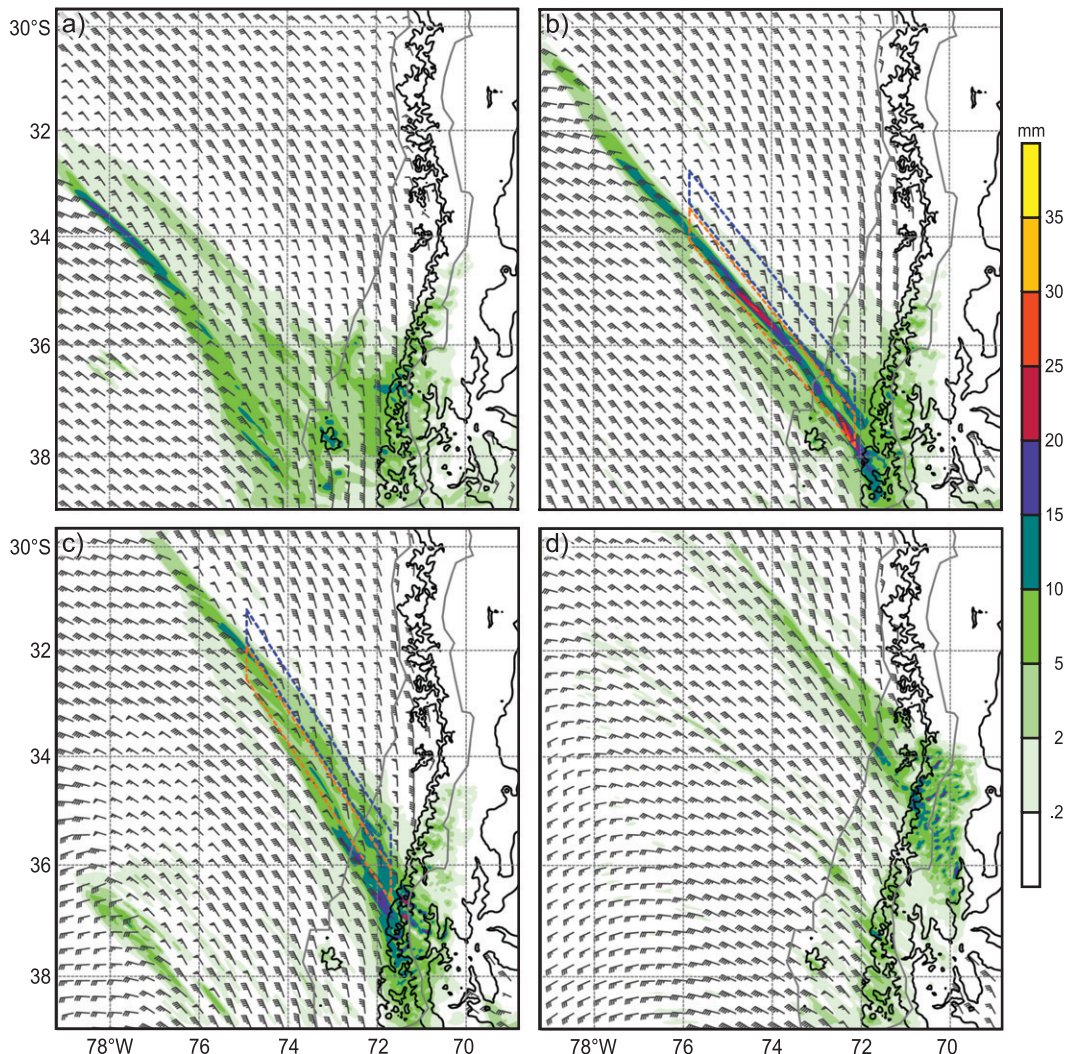


FIG. 18. As in Fig. 5, but for the RANDES simulation. Boxes in (b) and (c) are examples of the moving box where the frontogenesis and hydrometeor concentrations were calculated in the vicinity of the front in Figs. 20 and 21, respectively (orange dashed lines), and the hydrometeor concentrations were calculated ahead of the front in Fig. 22 (blue dashed lines).

front as it approached the continent and made landfall (see the orange dashed line boxes in Figs. 18b,c).

The calculated total frontogenesis and each of its contributor terms for the simulations are shown in Fig. 20. When the front approached the coast and made landfall, between 0000 and 0500 UTC, the convergence was similar in both the CTL and RANDES runs. After 0500 UTC, the total frontogenesis and convergence in the CTL run were higher than that in the RANDES run (although frontogenesis was larger just until 0900 UTC). During this landfalling stage, the tilting term was the major contributor to the frontogenesis, and the stretching deformation was the second in both runs. The diabatic term minimally contributed to frontogenesis and frontolysis, and the shearing deformation was negligible for both runs.

Although the tilting was a major frontogenetic term in both runs, there was no net difference in this term between the runs as it was highly variable in time. The tilting term was probably increased by mountain waves in the along-barrier direction produced by the barrier jet flowing over the corrugated coastal terrain of central Chile; such a process has already been observed on the Oregon coast of the United States affecting the precipitation distribution (Garvert et al. 2007). On the other hand, the stretching deformation term was always larger for the CTL compared to the RANDES during the landfalling stage, which is consistent with the convergence series having a greater difference in favor of the CTL run.

For all of the times in Fig. 20, the convergence, stretching deformation, and total frontogenesis decreased

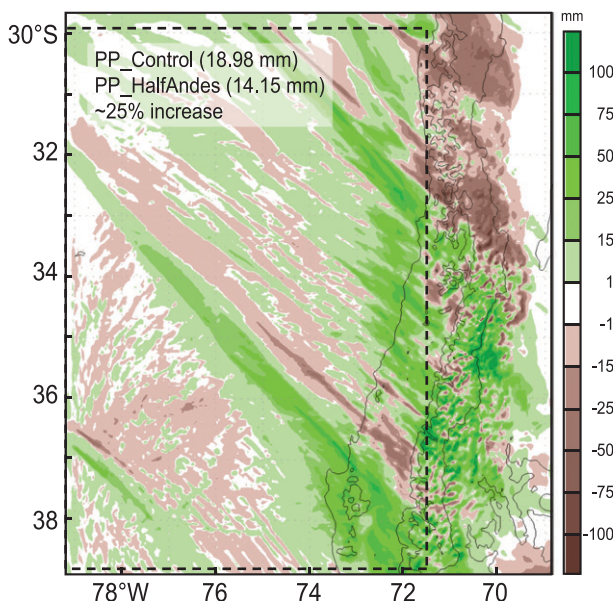


FIG. 19. Difference (CTL – RANDES simulation) in the 48-h accumulated precipitation (mm) from 0000 UTC 7 Jun to 0000 UTC 9 Jun 2006. Dashed lines enclose area where the mean upstream precipitation was calculated for both simulations.

by 12%, 27%, and 5%, respectively, in the RANDES run compared to that in the CTL run, while the tilting term increased by 7%. However, considering only the times between 0500 and 1200 UTC, after the front made landfall, the same three quantities decreased by 17%, 56%, and 13%, and tilting increased by 4% in the RANDES. These results indicate a major influence of the stretching deformation on the greater total frontogenesis in the CTL than in the RANDES run; and overall, supports the notion that a lower mountain range leads to less upstream precipitation from the front and the NCFR as a result of a reduced upstream blocking effect and low-level convergence.

To address the effect of the reduced Andes terrain on the seeder-feeder mechanism within the NCFR, we calculated mean hydrometeor concentrations within the same moving box surrounding the front as frontogenesis, and within a moving box surrounding the cloud deck just ahead of the front using the model data from the CTL and RANDES run (see the boxes in Figs. 18b,c). For the same times as frontogenesis calculation and within the frontal box shown in Fig. 21, the concentration of graupel above 2000 m and of rain below 2500 m were always higher in the CTL than in the RANDES run; while the concentration of cloud water and vapor in the whole atmosphere were lower in the CTL run. In total, the CTL run produced 32% more graupel and 9% more rain, and 0.5% and 4% less cloud water and vapor than the RANDES run, which suggests more riming and

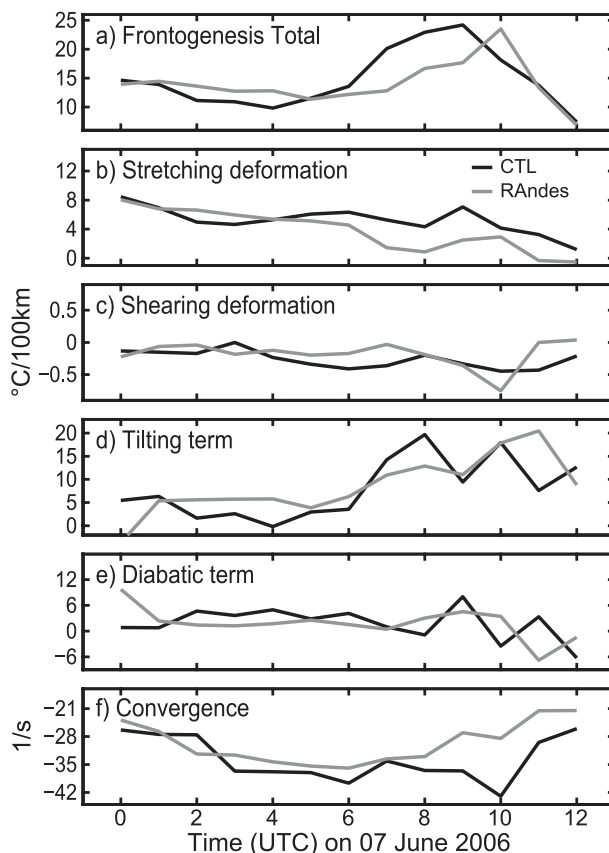


FIG. 20. Time series traces of the (a) total frontogenesis [$^{\circ}\text{C} (100 \text{ km h}^{-1})^{-1}$], (b) stretching deformation term, (c) shearing deformation term, (d) tilting term, (e) diabatic term, and (f) convergence (s^{-1}) for the CTL (black) and RANDES (gray) simulations. All quantities were averaged within a fixed-size box (20×60 grid points in the horizontal and the lowest 8 model vertical levels), which moved following the front from 0000 UTC 7 Jun to 1200 UTC 7 Jun 2006 (13 times, 1 per hour; see boxes with dashed orange lines in Fig. 18).

less cloud water and vapor removal processes within the front in the CTL run. Within the cloud deck located in the ahead-of-front box of Fig. 22, the CTL simulation produced 35% and 52% more snow and cloud ice particles above 2500 m, respectively, and 24% and 4% less cloud water and vapor in the whole atmosphere than the RANDES simulation (Fig. 22). These differences in hydrometeor concentrations between both simulations strongly suggest that a cloud deck in the ahead-of-front zone with more ice particles led to a more active riming process in the front for the CTL simulation.

6. Conclusions

This study has examined the influence of the Andes on the upstream precipitation associated with a deep

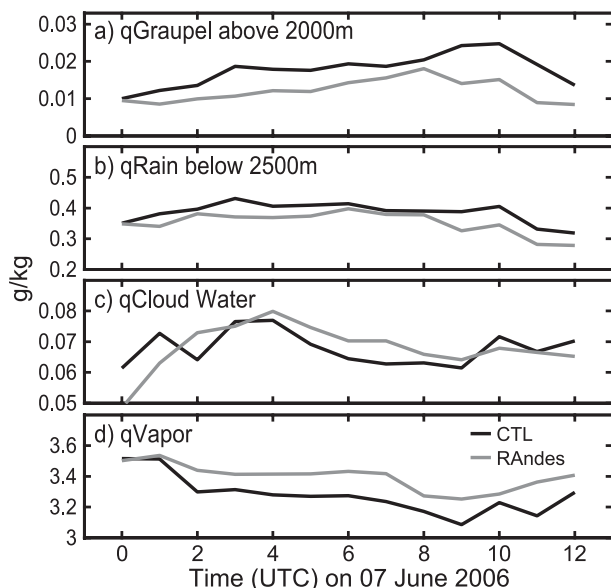


FIG. 21. Time series traces of the hydrometeor concentrations in the vicinity of the front showing (a) graupel above 2000 m; (b) rain below 2500 m; and (c),(d) cloud water and vapor in all levels of the atmosphere for the CTL (black lines) and RANdes (gray lines) simulations from 0000 UTC 7 Jun to 1200 UTC 7 Jun 2006. All quantities were averaged in a 20×60 grid point ($60 \times 480 \text{ km}^2$) box that moved following the front (see boxes with orange dashed lines in Fig. 18).

extratropical cyclone approaching from the southeastern Pacific with a strong cold front. The selected case study is representative of heavily precipitating winter storms characterized by an “atmospheric river” in the precold frontal environment. Previous investigations have shown that when the front and atmospheric river intersect a west coast mountain range, the precipitation is strongly enhanced in the region immediately upstream of the mountains (Neiman et al. 2008). When these storms strike the mountainous west coast of South America in the latitude range of $\sim(32^\circ\text{--}38^\circ\text{S})$, they can cause flooding, landslides, and avalanches (e.g., Viale and Nuñez 2011). A high-resolution WRF Model simulation and TRMM PR data show that the intense precipitation over central Chile and the adjacent Pacific Ocean in the selected case was produced primarily by a NCFR as it made landfall and moved equatorward between 7 and 8 June 2006. The model simulation indicates that the NCFR gradually increased its rainwater, graupel, and snow content, had stronger updrafts, and winds turning to a cross-front direction toward the front, as the distance from the cordillera decreased. Consequently, the NCFR produced higher rain accumulations over land just upstream of the Andes than over the open ocean. This simulated upstream enhancement of the NCFR extended to about 600 km west of the crest of the

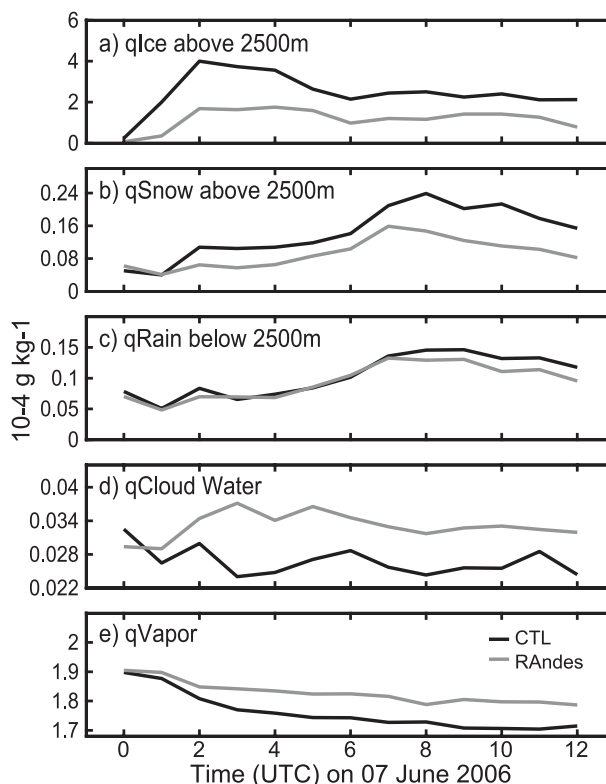


FIG. 22. As in Fig. 21, but for the ahead-of-front hydrometeor concentrations showing (a),(b) snow and cloud ice above 2500 m, and (c),(d) cloud water and vapor in all levels of the atmosphere for the CTL (black lines) and RANdes (gray lines) simulations from 0000 UTC 7 Jun to 1200 UTC 7 Jun 2006. All quantities were averaged in a 20×60 grid points ($60 \times 480 \text{ km}^2$) box that moved just ahead of the front (see boxes with blue dashed lines in Fig. 18).

Andes over the ocean, which denotes a prominent orographic effect on precipitation.

The mesoscale kinematics and microphysical analyses from the high-resolution simulation and the available observations, and the sensitivity experiment reducing the height of the Andes in the model presented in this study, allow us to infer physical mechanisms leading to the storm’s enhanced precipitation upstream of the Andes. The orographic enhancement process involves both low-level and midlevel orographically based processes. At low levels, orographically blocked flow ahead of the front enhanced low-level convergence when the front approached and thus enhanced the updrafts of the NCFR. Below the 0°C isotherm ($\sim 3000 \text{ m}$), these enhanced updrafts produced warm rain by coalescence. In addition, lifting of the moist atmospheric river upstream of the Andes produces midlevel stratiform clouds. This midlevel upstream orographic ascent of the atmospheric river is strong enough to produce snow aloft and light precipitation in the region ahead of the front. A seeder-feeder mechanism then becomes active when the NCFR

moves into the region occupied by the orographically enhanced midlevel stratiform cloud layer. The enhanced NCFR updrafts then rise into the orographically induced midlevel layer cloud and activate the seeder-feeder mechanism. The supercooled water produced and lofted by the updrafts into the lightly precipitating orographically induced atmospheric river cloud layer creates a feeder zone in midlevels, which is seeded by the snow particles of the midlevel orographically induced layer cloud. Within the resulting feeder-seeder zone inside the stratiform cloud, the snow particles in the layer cloud accrete the supercooled water of the enhanced NCFR updrafts and grow rapidly by riming to form graupel, which then falls out, melts, and contributes to the enhanced NCFR rain. The experiment artificially reducing the height of the Andes shows that the extreme height of the real mountain barrier strengthens frontogenesis and upstream blocking, which results in an enhanced seeder-feeder process occurring at midlevels in the case of the taller Andes compared to lower mountain ranges such as those of the west coast of North America. The higher Andes thus produce stronger frontal lifting and slow down the frontal system even more so that the processes become more robust and operate over a longer time to produce more rain on the windward side.

The findings of this study are entirely consistent with previous investigations of frontal systems accompanied by prefrontal atmospheric rivers approaching the west coasts of central Chile and the western region of the United States, similar to that seen in the case analyzed here. These storms are well known to enhance the rainfall upstream of where the atmospheric rivers intersect coastal mountain ranges. Our results now further indicate that the set of cooperative frontal and orographic processes are involved in the physical mechanisms of precipitation enhancement. Low-level blocking enhances the frontal updrafts interacting with an orographically produced midlevel cloud layer to form a robust feeder-seeder process, and this effect is maximized in the case of the Andes as a result of their great height. The frequent occurrence of these orographically enhanced storms in both hemispheres suggests that the mechanisms identified here have wide applicability and need to be accounted for accurately in models for both forecasting and climatologically assessing the hydrometeorology of the west coastal regions of both North and South America.

Acknowledgments. The authors would like to acknowledge Socorro Medina for logistical assistance and Greg Thompson for helpful advice regarding microphysics scheme details. We also thank the anonymous reviewers for their detailed and insightful comments.

Stacy Brodzik and Beth Tully gave valuable support in processing the data and graphics used in this study. Humberto Fuenzaldia helped in obtaining surface data. This research was supported by National Science Foundation Grants AGS-0820586 and AGS-1144105, NASA Grant NNX10AH70G, and the Consejo Nacional de Investigaciones Científicas y Tecnológicas (CONICET) de Argentina.

REFERENCES

- Barrett, B. S., R. D. Garreaud, and M. Falvey, 2009: Effect of the Andes Cordillera on precipitation from a midlatitude cold front. *Mon. Wea. Rev.*, **137**, 3092–3109.
- Bond, N. A., and Coauthors, 1997: The Coastal Observations and Simulations with Topography (COAST) experiment. *Bull. Amer. Meteor. Soc.*, **78**, 1941–1955.
- Chen, F., and J. Dudhia, 2001: Coupling an advanced land-surface/hydrology model with the Penn State/NCAR MM5 modeling system. Part I: Model description and implementation. *Mon. Wea. Rev.*, **129**, 569–585.
- Colle, B. A., C. F. Mass, and B. F. Smull, 1999: An observational and numerical study of a cold front interacting with the Olympic Mountains during COAST IOP5. *Mon. Wea. Rev.*, **127**, 1310–1334.
- , B. F. Smull, and M. Yang, 2002: Numerical simulations of a landfalling cold front observed during COAST: Rapid evolution and responsible mechanisms. *Mon. Wea. Rev.*, **130**, 1945–1966.
- Doyle, J. D., 1997: The influence of mesoscale orography on a coastal jet and rainband. *Mon. Wea. Rev.*, **125**, 1465–1488.
- Dudhia, J., 1989: Numerical study of convection observed during the winter monsoon experiment using a mesoscale two-dimensional model. *J. Atmos. Sci.*, **46**, 3077–3107.
- Durrán, D. R., and J. B. Klemp, 1982: The effects of moisture on the Brunt–Väisälä frequency. *J. Atmos. Sci.*, **39**, 2152–2158.
- Falvey, M., and R. Garreaud, 2007: Wintertime precipitation episodes in Central Chile: Associated meteorological conditions and orographic influences. *J. Hydrometeorol.*, **8**, 171–193.
- Garvert, M. F., B. Smull, and C. Mass, 2007: Multiscale mountain waves influencing a major orographic precipitation event. *J. Atmos. Sci.*, **64**, 711–736.
- Hobbs, P. V., and K. R. Biswas, 1979: The cellular structure of narrow cold-frontal rainbands. *Quart. J. Roy. Meteor. Soc.*, **105**, 723–727.
- , and O. G. Persson, 1982: The mesoscale and microscale structure and organization of clouds and precipitation in midlatitude cyclones. Part V: The substructure of narrow cold-frontal rainbands. *J. Atmos. Sci.*, **39**, 280–295.
- Hong, S. Y., Y. Noh, and J. Dudhia, 2006: A new vertical diffusion package with an explicit treatment of entrainment processes. *Mon. Wea. Rev.*, **134**, 2318–2341.
- Houze, R. A., Jr., 1993: *Cloud Dynamics*. Academic Press, 573 pp.
- , 2012: Orographic effects on precipitating clouds. *Rev. Geophys.*, **50**, RG1001, doi:10.1029/2011RG000365.
- , P. V. Hobbs, K. R. Biswas, and W. M. Davis, 1976: Mesoscale rainbands in extratropical cyclones. *Mon. Wea. Rev.*, **104**, 868–878.
- Iguchi, T., T. Kozu, R. Meneghini, J. Awaka, and K. Okamoto, 2000a: Rain-profiling algorithm for the TRMM Precipitation Radar. *J. Appl. Meteor.*, **39**, 2038–2052.
- , R. Meneghini, J. Awaka, T. Kozu, and K. Okamoto, 2000b: Rain-profiling algorithm for the TRMM Precipitation Radar data. *Adv. Space Res.*, **25**, 973–976.

- James, P. K., and K. A. Browning, 1979: Mesoscale structure of line convection at surface cold fronts. *Quart. J. Roy. Meteor. Soc.*, **105**, 371–382.
- Kain, J. S., and J. M. Fritsch, 1993: Convective parameterization for mesoscale models: The Kain–Fritsch scheme. *The Representation of Cumulus Convection in Numerical Models, Meteor. Monogr.*, No. 46, Amer. Meteor. Soc., 165–170.
- Kessler, E., and R. Wexler, 1960: Observations of a cold front, 1 October 1958. *Bull. Amer. Meteor. Soc.*, **41**, 253–257.
- Liu, C., K. Ikeda, G. Thompson, R. Rasmussen, and J. Dudhia, 2011: High-resolution simulations of wintertime precipitation in the Colorado Headwaters region: Sensitivity to physics parameterization. *Mon. Wea. Rev.*, **139**, 3533–3553.
- Marwitz, J. D., 1987: Deep orographic storms over the Sierra Nevada. Part I: Thermodynamic and kinematic structure. *J. Atmos. Sci.*, **44**, 159–173.
- Matejka, T. J., R. A. Houze Jr., and P. V. Hobbs, 1980: Microphysics and dynamics of the clouds associated with mesoscale rainbands in extratropical cyclone. *Quart. J. Roy. Meteor. Soc.*, **106**, 29–56.
- Medina, S., and R. A. Houze Jr., 2003: Air motions and precipitation growth for orographic precipitation enhancement. *Quart. J. Roy. Meteor. Soc.*, **129**, 345–371.
- , B. F. Smull, R. A. Houze Jr., and M. Steiner, 2005: Cross-barrier flow during orographic precipitation events: Results from MAP and IMPROVE. *J. Atmos. Sci.*, **62**, 3580–3598.
- Miller, J. E., 1948: On the concept of frontogenesis. *J. Meteor.*, **5**, 169–171.
- Minder, J. R., D. R. Durran, and G. H. Roe, 2011: Mesoscale controls the mountainside snow-line. *J. Atmos. Sci.*, **68**, 2107–2127.
- Mlawer, E. J., S. J. Taubman, P. D. Brown, M. J. Iacono, and S. A. Clough, 1997: RRTM, a validated correlated-k model for the longwave. *J. Geophys. Res.*, **102** (D14), 16 663–16 682.
- Neiman, P. J., P. O. G. Persson, F. M. Ralph, D. P. Jorgensen, A. B. White, and D. E. Kingsmill, 2004: Modification of fronts and precipitation by coastal blocking during landfalling winter storm in Southern California: Observations during CALJET. *Mon. Wea. Rev.*, **132**, 242–273.
- , F. M. Ralph, G. A. Wick, J. D. Lundquist, and M. D. Dettinger, 2008: Meteorological characteristics and overland precipitation impacts of atmospheric rivers affecting the west coast of North America based on eight years of SSM/I satellite observations. *J. Hydrometeor.*, **9**, 22–47.
- Paulson, C. A., 1970: The mathematical representation of wind speed and temperature profiles in the unstable atmospheric surface layer. *J. Appl. Meteor.*, **9**, 857–861.
- Pierrehumbert, R. T., and B. Wyman, 1985: Upstream effects of mesoscale mountains. *J. Atmos. Sci.*, **42**, 977–1003.
- Ralph, F. M., and Coauthors, 1999: The California Land-falling Jets Experiment (CALJET): Objectives and design of a coastal atmosphere-ocean observing system deployed during a strong El Niño. Preprints, *Third Symp. on Integrated Observing Systems*, Dallas, TX, Amer. Meteor. Soc., 78–81.
- , P. J. Neiman, and G. A. Wick, 2004: Satellite and CALJET aircraft observations of atmospheric rivers over the eastern North Pacific Ocean during the winter of 1997/98. *Mon. Wea. Rev.*, **132**, 1721–1745.
- Rotunno, R., J. B. Klemp, and M. L. Weisman, 1988: A theory for strong, long-lived squall lines. *J. Atmos. Sci.*, **45**, 463–485.
- Rutledge, S. A., and P. V. Hobbs, 1983: The mesoscale and microscale structure and organization of clouds and precipitation in midlatitude cyclones. VIII: A model for “seeder-feeder” process in warm-frontal rainbands. *J. Atmos. Sci.*, **40**, 1185–1206.
- , and —, 1984: The mesoscale and microscale structure and organization of clouds and precipitation in midlatitude cyclones. XII: A diagnostic modeling study of precipitation development in narrow cold-frontal rainbands. *J. Atmos. Sci.*, **41**, 2949–2972.
- Saha, S., and Coauthors, 2010: The NCEP Climate Forecast System Reanalysis. *Bull. Amer. Meteor. Soc.*, **91**, 1015–1057.
- Skamarock, W. C., J. B. Klemp, J. Dudhia, D. O. Gill, D. M. Barker, W. Wang, and J. G. Powers, 2008: A description of the Advanced Research WRF version 3. NCAR Tech. Note NCAR/TN-475+STR, 125 pp.
- Thompson, G., P. R. Field, R. M. Rasmussen, and W. D. Hall, 2008: Explicit forecast of winter precipitation using an improved bulk microphysics scheme. Part II: Implementation of a new snow parameterization. *Mon. Wea. Rev.*, **136**, 5097–5115.
- Viale, M., and F. A. Norte, 2009: Strong cross-barrier flow under stable conditions producing intense winter orographic precipitation: A case study over the subtropical Central Andes. *Wea. Forecasting*, **24**, 1009–1031.
- , and M. N. Nuñez, 2011: Climatology of winter orographic precipitation over the subtropical Central Andes and associated synoptic and regional characteristics. *J. Hydrometeor.*, **12**, 481–507.
- Yu, C.-K., and B. F. Smull, 2000: Airborne Doppler observations of a landfalling cold front upstream of steep coastal orography. *Mon. Wea. Rev.*, **128**, 1577–1603.
- Zhu, Y., and R. E. Newell, 1998: A proposed algorithm for moisture fluxes from atmospheric rivers. *Mon. Wea. Rev.*, **126**, 725–735.